JGR Oceans

RESEARCH ARTICLE
10.1029/2021JC017393

Volume Transport Time Series and Variability of the North Atlantic Eastern Boundary Current at Goban Spur

Martin Moritz[1], Kerstin Jochumsen[1], Dagmar Kieke[2,3], Birgit Klein[1], Holger Klein[1], Manuela Köllner[1], and Monika Rhein[2,3]

[1]Federal Maritime and Hydrographic Agency (BSH), Hamburg, Germany, [2]Institute of Environmental Physics, University of Bremen, Bremen, Germany, [3]MARUM-Center for Marine Environmental Sciences, University of Bremen, Bremen, Germany

Key Points:

- The analysis of multiplatform observational efforts is used to study the circulation at the North Atlantic Eastern Boundary
- The volume transport of the offshore branch of the European Shelf Current is on average 3.2 ± 0.4 Sv for the period 1993–2019
- Transport variability is in the range of −7.5–15.7 Sv and induced by eddies and meandering North Atlantic Current branches

Correspondence to:
M. Moritz,
martin.moritz@bsh.de

Citation:
Moritz, M., Jochumsen, K., Kieke, D., Klein, B., Klein, H., Köllner, M., & Rhein, M. (2021). Volume transport time series and variability of the North Atlantic eastern boundary current at Goban Spur. *Journal of Geophysical Research: Oceans*, *126*, e2021JC017393. https://doi.org/10.1029/2021JC017393

Received 23 MAR 2021
Accepted 8 JUL 2021

Abstract The Eastern Boundary Current is an essential part of the water mass exchange between the subtropical and subpolar North Atlantic. Here, we study the offshore branch of the European Shelf Current (ESC) over the Goban Spur slope area off Ireland. Our analysis is based on current measurements obtained from a multiyear mooring effort, complemented by ship-board observations along a hydrographic section, satellite-derived estimates of absolute dynamic topography with geostrophic currents, and float trajectories. These data serve to quantify the offshore branch of the ESC on intraannual to interannual timescales. From the moored observations, we derive a mean poleward along-slope volume flux of 3.7 ± 0.7 Sv for the period 2017–2019. Using a multilinear regression model and geostrophic surface velocities, we extend the time series to the period 1993–2019 and obtain a long-term mean transport of 3.2 ± 0.4 Sv. Both time series show strong variability ranging from −7.5 to 15.7 Sv. The variability is linked to a dynamic eddy field, especially a stationary cyclonic circulation pattern near the mooring array, and meandering of current branches originating from the North Atlantic Current.

We find no evidence of a consistent deep boundary current extending from the shelf break to the position of the offshore mooring (4,500 m depth), but confirm a persistent along-slope flow at the shallower slope (1,500 m depth). Geostrophic surface velocities and float trajectories reveal that the offshore branch of the ESC does not follow a clear northward path from the eastern subtropical regions but rather indicate the intermittent character of the flow.

Plain Language Summary In this study, we describe the European Shelf Current (ESC) in the eastern North Atlantic. The study area is the deeper part of the Goban Spur area off Ireland. We use current measurements of instruments deployed in the water column from 2016 to 2019 combined with satellite observations of surface circulation and drifting float paths. We aim to quantify the contribution of the offshore branch to the ESC system. We calculate a poleward volume transport following the slope that is on average 3.7 ± 0.7 Sverdrup (Sv; 1 Sv = 1 million cubic meter per second) for the period 2017–2019. We use a mathematical relation between mooring data and satellite observations to extend the time series to the period 1993–2019 and obtain an average transport of 3.2 ± 0.4 Sv. There occur strong changes over time ranging from −5 to 15 Sv. These changes are caused by rotating vortices (eddies), especially a counter-clockwise rotating circulation pattern near the moorings, and changing positions of currents branching from the North Atlantic Current. We find that the offshore branch of the ESC does not follow a clear northward path from the eastern subtropical regions of the North Atlantic. Instead, the flow is of rather unsteady character.

1. Introduction

The circulation along the European continental slope is determined by the confluence of two major current systems forming the complex European Boundary Current System. Warm and saline water masses from the subtropical gyre (STG) carried within the northern part of the gyre interact with the colder and fresher water masses from the subpolar gyre (SPG), brought to the region by its southern branch. A connecting feature of both gyres is the North Atlantic Current (NAC), which contributes through its different branches to both gyres and includes the Subpolar Front. Recently, Stendardo et al. (2020) and Nowitzki et al. (2021) found and quantified a direct pathway of NAC water that leads from the location of the Mann eddy in the

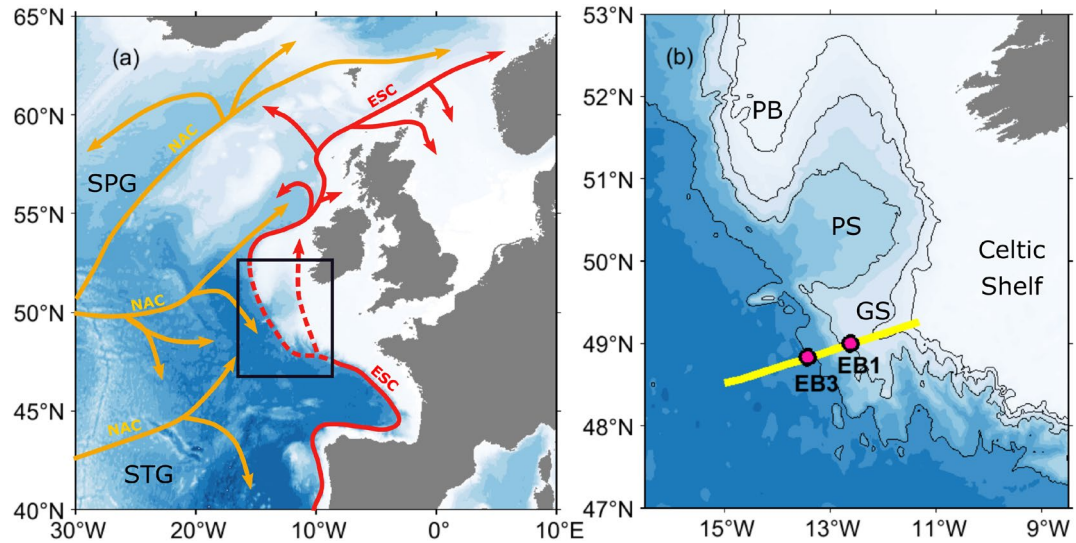

Figure 1. Map of (a) the Eastern North Atlantic and simplified main circulation with the region of Goban Spur highlighted by the black rectangle and (b) positions of moorings EB1 and EB3. The dashed red line in (a) highlights the uncertainty in the continuity of the northward pathway of the European Shelf Current (ESC) that is discussed in this study. Black contour lines in (b) show 500 m, 1,000 m, 2,000 m, and 4,000 m isobaths, the yellow line indicates the cruise track across the mooring array. ESC, European Slope Current; NAC, North Atlantic Current; SPG, Subpolar Gyre; STG, Subtropical Gyre; GS, Goban Spur; PB, Porcupine Bank; PS, Porcupine Seabight.

Newfoundland Basin (about 42°N/42°W) into the eastern subpolar North Atlantic. The extension of the warm water pathway out of the STG northwards along the eastern boundary depends on the contraction or expansion of the SPG (e.g., Häkkinen & Rhines, 2009; Holliday et al., 2020; Pingree, 2005).

A prominent route of subtropical water masses along the eastern boundary of the North Atlantic is via the European Slope Current (ESC), which is thought to follow the continental shelf break off Portugal as far as the Norwegian Sea (e.g., Pingree & Le Cann, 1989, 1990). This current has been observed at different locations along the European slope, but the focus was generally on water depths shallower than 1,000 m (e.g., Pingree et al., 1999; van Aken et al., 2005), where it was often termed simply "slope current" (e.g., Pingree et al., 1999) or "shelf-edge current" (e.g., White & Bowyer, 1997). A consistent terminology and circulation scheme for the northward flow in this region is presently lacking in the published literature. At the Celtic shelf and slope, the current typically has a strength of 10 cm s^{-1} in the upper water column and reaches about 40 cm s^{-1} at maximum (Pingree et al., 1999).

Although the northward flow along the European slope is described as continuous (e.g., Pingree et al., 1999), drifter trajectories clearly indicate eddy stirring away from the boundary (Pingree, 1993; van Aken, 2002). Due to undulations of the shelf edge with deep canyons cutting into the slope, eddy formation may be triggered by flow-topography interaction or overshooting at topographic obstacles (e.g., Huthnance et al., 2001). The generally topography-bound flow can thus detour into the interior before returning toward the eastern boundary (e.g., Ullgren & White, 2010).

In this work, we term the northward along-slope current ESC, and its location and course are schematically summarized in Figure 1. We refer to its shallower part as the Shelf Edge Current (SEC), while we label the offshore part "deep Eastern Boundary Current (deep EBC)." As we will show in our study, this current component is centered over the deep part of the continental slope, that is, above 2,000–4,000 m water depth. In contrast to the shallow part of the current system, the deep EBC has been hardly addressed so far. A northward current core of the ESC that is adjacent to the seabed of the upper slope is termed undercurrent (UC) and has been described by Reid (1979), New et al. (2001), and McCartney and Mauritzen (2001).

The monitoring introduced in this study focuses on the ESC at Goban Spur, a topographic feature extending away from the southwestern Celtic shelf into the deeper ocean. Here, the transition region from the STG to the SPG leads to weak average currents; also a local minimum in tidal energy is present (Huthnance

et al., 2001). Our observations have been obtained from two deep-sea moorings (Figure 1b), which represent the eastern extension of the basin-wide "North Atlantic Changes" (NOAC) ocean observatory deployed along 47°/48°N (Frajka-Williams et al., 2019; McCarthy et al., 2020; Nowitzki et al., 2021; Rhein et al., 2019). The NOAC array is located in a region where the interior velocity profile is correlated to the geostrophic surface currents observed by altimetry (Nowitzki et al., 2021; Rhein et al., 2019; Roessler et al., 2015; Stendardo et al., 2020).

The goal of our study is to determine time series of volume fluxes as well as to describe the major features and properties of the flow and its variability at the eastern slope. The main focus lies on the strength and persistence of the deep EBC and the net transport to the north. In the following, we introduce our data set consisting of velocity time series obtained from deep-sea moorings, property distributions from four ship surveys, large-scale distributions of absolute dynamic topography and sea surface velocities obtained from satellite altimetry as well as Argo float trajectories (Section 2). Then, we give a descriptive view of the general features that define the hydrographic composition of the water column as well as the current system at Goban Spur based on observational efforts accomplished between 2016 and 2019 (Section 3). We start the results section by presenting the mooring records and discuss similarities and notable differences in the various velocity records obtained at the two mooring sites (Section 4). We derive spatial and temporal patterns in the velocity records and infer times series of the volume transport representing the strength of the deep EBC throughout the mooring period. These transports are further extended in time by applying a multilinear regression model that connects the 2-year mooring record to 27 years of altimetry-derived surface geostrophic velocities. Finally, we close by discussing our results in the light of interactions between the flow field along the eastern boundary and the larger-scale circulation and bring our description of the state of the boundary current circulation at Goban Spur into context to other published results (Section 5). Additionally, we tackle the question of exchange between the STG and SPG by including Argo float trajectories and satellite altimetry, thus expanding the local scope of mooring data to a regional perspective.

2. Data

2.1. The Eastern Boundary Array: Mooring Design and Instrumentation

The data analyzed in this study have been obtained from deep-sea moorings deployed in the eastern boundary (EB) region along the crest of Goban Spur (Figure 1). Originally, three moorings were planned, called EB1, EB2, and EB3. These were supposed to span the deep EBC between the 1,500 and 4,400 m isobaths. The shallower part of the continental slope exhibits high fishing activity (Witt & Godley, 2007). To prevent mooring losses the shallow SEC region was thus not included in the EB mooring array. Due to mooring losses in 2017, only the moorings EB1 and EB3 have been redeployed since 2017. The center location between the two moorings (i.e., the previous EB2 mooring site) is thus not covered. The two moorings EB1 and EB3 are located 62 km apart. Between 2016 and 2019 both moorings were serviced on an annual basis with recovery/deployment cruises typically conducted in spring to early summer. Table 1 summarizes the deployment locations and periods of both moorings as well as identifiers of the involved ship cruises and depth levels of current meters. In this study, we discuss data obtained from mooring EB1 in the period April 2016–May 2019 and from EB3 in the period June 2017–May 2019.

The mooring designs involved acoustic current meters of type Aanderaa Seaguard RCM DW (SG; only mooring EB3), Nortek Aquadopp Deepwater 6000 (AQD), and Teledyne-RD Instruments Workhorse Longranger Acoustic Doppler Current Profiler (LR; only mooring EB1), the latter operated in an upward looking orientation. While the first two current meter types delivered single-point measurements, the LR was programmed to measure velocity and direction in 16 m bins for a maximum distance of 500 m from the instrument. The SGs recorded at a sampling rate of 60 min, AQD and LR current meters were set to 30 min sampling intervals. The instrument error for a single velocity measurement was 1.0 cm s^{-1} (SG) and 1.5 cm s^{-1} (AQD and LR).

Both moorings carried additional temperature and salinity sensors. Since our focus is on the velocity records obtained from the EB mooring array, the analysis of the T/S data is not part of this study. The design of mooring EB3 was altered slightly after each deployment according to instrument availability and scientific analyses, thus instruments were installed at partly different nominal depths during the different mooring

Table 1
Locations, Current Meter Depths, and Respective Deployment Information of the Two Deep-Sea Moorings EB1 and EB3 Installed Along the Crest of Goban Spur During 2016 and 2019

Mooring	Latitude	Longitude	Depth (m)	Current meter depths (m)	Deployment (Cruise)	Recovery (Cruise)	Record length (days)
EB1/1	49°00.02′N	12°37.08′W	1,530	208–720 (LR) 1,062/1,379 (AQD)	April 4, 2016 (MSM53)	June 3, 2017 (MSM64)	426
EB1/2	49°00.02′N	12°37.08′W	1,530	208–720 (LR) 1,084/1,405 (AQD)	June 4, 2017 (MSM64)	April 11, 2018 (MSM73)	312
EB1/3	49°00.03′N	12°37.14′W	1,534	154–730 (LR) 1,067/1,389 (AQD)	April 12, 2018 (MSM73)	May 23, 2019 (MSM83)	407
EB3/1	48°49.98′N	13°25.98′W	4,453	no data	April 5, 2016 (MSM53)	Lost (MSM64)	no data
EB3/2	48°49.98′N	13°25.98′W	4,453	409/710/1,223/1,725 2,239/2,743/3,275/3,791	June 5, 2017 (MSM64)	April 11, 2018 (MSM73)	310
EB3/3	48°49.98′N	13°25.98′W	4,453	458/757/1,256/1,764 2,268/2,770/3,268/3,786	April 11, 2018 (MSM73)	May 23, 2019 (MSM83)	408

Note. At mooring EB1, one upward looking LR was deployed, all other current meters were of type AQD; all current meters installed at mooring EB3 were of type SG. See text for details.
AQD, aquadopp deepwater; EB, eastern boundary; LR, longranger; SG, seaguard.

periods (see Table 1 and appendix Figure A1). The deepest and shallowest levels of current measurements were at about 1,400 and 200 dbar at mooring EB1 and at about 3,800 and 400 dbar at mooring EB3 (Table 1).

The actual instrument positions of all current meters were determined from pressure records. For instruments without particular pressure sensors the pressure time series were obtained from pressure data measured above or below the nominal depth of the sensor. For each device carrying a pressure sensor the difference between nominal pressure and mean pressure was calculated and interpolated vertically to obtain the deviation from nominal depth, that is, the mean nominal pressure ($\overline{p}$) of instruments without pressure sensors. Finally, we assumed that $p(t) = \overline{p} + p(t)'$, where p' was taken from the nearest instrument with pressure sensor.

During the EB3 mooring period 2017/2018 the SG velocity measurements at 710 m were identified to be faulty. However, during the second EB3 mooring period 2018/2019 the flow measured by a SG at a similar depth (757 m) was found to be highly correlated ($r > 0.9$) with records from a shallower device installed at 458 m (explained variance > 80% for both velocity components). We then re-constructed the time series of u and v at 757 m by linear regression and compared them with the original measurements at this depth, which led to an overall good agreement within 1 cm s^{-1} on average, with rare deviations in the order of 5–10 cm s^{-1}. Thus, we applied this approach for the period 2017/2018 to reconstruct velocities at 710 m from the current meter installed at 409 m.

The original sampling intervals ranging from 5 to 60 min were interpolated on a regular hourly time grid. The current meter records were corrected for the local magnetic declination using the IGRF12 model (Erwan et al., 2015). Since tidal and inertial periods are not targeted in this study, time series were low-pass filtered with a fourth order Butterworth filter with a 40-h cutoff period. All time series were symmetrically padded at the endpoints to reduce contamination by edge effects. Then, daily averages were calculated, reducing the error of the daily mean to 0.2 cm s^{-1} (SG) at EB3 and 0.3 cm s^{-1} (LR and AQD) at EB1. Finally, the u and v components of both moorings were interpolated vertically onto a regular pressure grid with 50 dbar increments. Vertical displacement (blow-downs) of the moorings with a range of 20–50 dbar occurred sporadically at EB3. These effects were compensated by the vertical interpolation.

2.2. Ship-Based Observations During 2016–2019

CTD and Lowered Acoustic Doppler Current Profiler (LADCP) profiles were collected on four annual transects during cruises with RV Maria S. Merian (see Table 1). All sections started on the shallow shelf to the east of 11°30′W (water depth of about 200 m) and followed the crest of Goban Spur to 15°W and beyond into the deep Atlantic. Consequently, they covered the shelf edge, slope and deep part of Goban Spur and the locations of the EB mooring sites (Figure 1b). Depending on the particular cruise, between 14 and 27 CTD/LADCP stations were carried out between 11°W and 15°W. The mean station distance of the individual cruises ranged from 5 to about 10 nm.

During all cruises, we used the same CTD-system of type SBE 9/11plus, attached to a carousel water sampler. CTD-derived conductivity was calibrated against in situ water samples using a salinometer and calibrated IAPSO standard seawater samples. The salinity uncertainty of the CTD system for all cruises was in the range 0.002–0.003. Practical salinity, potential temperature and potential density anomalies were derived using the MATLAB Gibbs Seawater toolbox version 3.06 (McDougall & Barker, 2011).

Current velocity at each CTD station was obtained from two LADCP devices of type Teledyne-RD Instruments Workhorse Monitor operating at a frequency of 300 kHz. Both were attached to the water sampler and were operated in a synchronized mode with the downward-looking device triggering the upward-looking instrument. Both devices were set to a ping rate of 1 Hz and 10 m depth bins. During the first two cruises conducted in 2016 and 2017, the LADCP-toolbox of the University of Bremen was used for the postprocessing of the raw data. In 2018 and 2019, the raw data were processed with the LDEO LADCP software (Thurnherr, 2018). Processing of despiked data in both cases followed methods outlined by Visbeck (2002) and was based on an inverse method incorporating the bottom track velocities. CTD time-series at 1 Hz resolution were incorporated into the LADCP data processing. During 2018 and 2019, data from a vessel-mounted ADCP of type Teledyne-RD Instruments Ocean Surveyor operated at 75 kHz (OS75) recorded at each CTD/LADCP station was included to improve the inverse solution in the upper part of the water column. Uncertainties of the resulting LADCP-derived velocity profiles fell into the range 3.0–5.3 cm s^{-1}.

The effect of tides on the LADCP observations was eliminated by using the TPXO7.2 tidal model (Egbert & Erofeeva, 2002) to estimate and remove the barotropic tides for the timing and location of each profile. Tidal velocities were generally in the range ±5 cm s^{-1}, while in the shallow shelf region (at water depth <500 m) they amounted up to ±13 cm s^{-1}. All CTD and LADCP profiles were interpolated vertically on a regular pressure grid with 10 dbar increments and horizontally with a 0.125° (≈5 nm) longitudinal spacing. The detided LADCP derived horizontal velocity components were subsequently rotated clockwise by 48° to obtain along- and cross-slope components. The choice of this angle will be motivated later in the text.

2.3. Wind Field in the Goban Spur Area During the Mooring Period

In order to relate our mooring results to the wind forcing, we use nearsurface (10 m) wind data from the ERA5 reanalysis single-level product (Copernicus Climate Change Service (C3S), 2017). Wind data are distributed on a 0.25° × 0.25° grid at hourly resolution. We calculated daily averages for the mooring period ranging from April 2016 to May 2019 for a box surrounding our mooring locations, that is, 48°30′N to 49°30′N and 12°W to 14°W including 14 grid points. From this box, we obtained a single wind time series by calculating the mean wind within the box. For comparison with the mooring records, the time series were low-pass filtered with a similar fourth order Butterworth filter.

2.4. Satellite Altimetry

Considering the large-scale perspective of our mooring results, we use satellite altimetry data provided by the Copernicus Marine Environmental Monitoring Service (CMEMS). In particular, we have analyzed gridded fields of reprocessed delayed-time (DT) L4 absolute dynamic topography (ADT) and corresponding surface geostrophic velocities (CMEMS product identifier SeaLevel_GLO_PHY_L4_REP_008_047, SSALTO/DUACS DT-2018). Starting in 1993 and ongoing, these data are provided on a 0.25° × 0.25° Cartesian

grid at daily resolution. Taburet et al. (2019) summarize the data processing steps and the corresponding data improvements on the latest DT-2018 product used here.

In order to evaluate the impact of potential eddies prevailing at the mooring sites, we additionally exploit the Mesoscale Eddy Trajectory Atlas (META) obtained from AVISO+ (Archivage, Validation et Interprétation des données des Satellites Océanographiques). This data set provides information inferred from sea surface altimetry on individually identified eddies, that is, their respective trajectories, radius, sense of rotation, and amplitude with respect to the sea level anomaly difference between the eddy's center and its edge. We use the delayed-time version 2.0 data set (META2.0 DT) that is presently available for the altimeter period starting on January 1, 1993 to March 7, 2020 and builds on the DT-2018 altimeter product. The eddy-tracking algorithm follows methods outlined by Chelton et al. (2011), Williams et al. (2011), and Schlax and Chelton (2016). The major steps to create META are presented in the data set documentation (AVISO, 2021).

2.5. Argo Float Trajectories From the Eastern Boundary Region

Additional information on advection pathways in the area of interest was obtained from investigating trajectories derived from profiling Argo floats. The majority of the Argo floats drifts at a depth of 1,000 m (typical parking depth between the profiles). The trajectories from the 10-day surfacing positions thus reflect the advection field at 1,000 m depth.

The trajectory analysis was performed on a subset of the global Argo data set downloaded from the Coriolis data center in August 2019. The downloaded global index file served as the basis for the inventory of all available data and to select floats within the Atlantic sector (Argo, 2019). The automated quality control of the Argo data system checks position and time quality and assigns quality flags to position and time. Only data (real time and delayed mode) with a quality flag equal to 1 ("good") for this type of information were used.

For our analysis on the continuity of the boundary current, we split the eastern boundary into three sections by defining boxes along the shelf. The boundary of all boxes is defined by the 1,000 m and 4,500 m contour using the Earth Topography Five Minute grid (ETOPO5; NOAA, 1988). The northern box ends at 54°30′N and is separated from box II around Goban Spur at 51°N. The southern box ends at 40°N and is separated from box II at 9°W. Only those Argo floats from the years 2016–2019 that passed through any of the three boxes stretching along the eastern boundary are considered here.

3. Hydrographic Setting and Flow Field at Goban Spur During 2016–2019

Composite plots of temperature, salinity and potential vorticity (PV) sections obtained during the four cruises are shown in Figure 2 (see appendix, Figure B1, for individual sections). Potential vorticity was calculated from $PV = \frac{f}{g}N^2$, where N^2 is the buoyancy frequency, f is the Coriolis parameter, and g is the gravitational acceleration. Water masses are identified most clearly by combining density ranges with the PV distribution (Figure 2c, see labels). In general, we follow water mass definitions presented by Stendardo et al. (2015) for the upper and intermediate ocean in this region that are combined in Table 2 with common definitions for the Labrador Sea Water (LSW).

At Goban Spur, PV is low in the upper part of the water column and beneath the surface layer (Figure 2) and associated with the presence of Subpolar Mode Water (SPMW). A high PV layer is located between about 500–1,000 dbar. Following Stendardo et al. (2015), the upper part of this layer is formed of Intermediate Water (IW). The lower part can be attributed to Mediterranean Outflow Water (MOW) that is known to propagate north along the eastern boundary of the Atlantic (Iorga & Lozier, 1999) and agrees with the salinity maximum observed on the Goban Spur section. However, the lateral position, extension and thickness of the high salinity layer varies throughout the individual repeated sections. Occasionally, this water mass is detached from the slope, crossing the positions of the moorings EB1 and EB3. In spring 2016, a separated saline patch was also identified west of EB3 in this depth range (Figure B1b). This offshore salinity maximum was presumably caused by detached eddies carrying MOW into the interior basin or by a recirculating current branch.

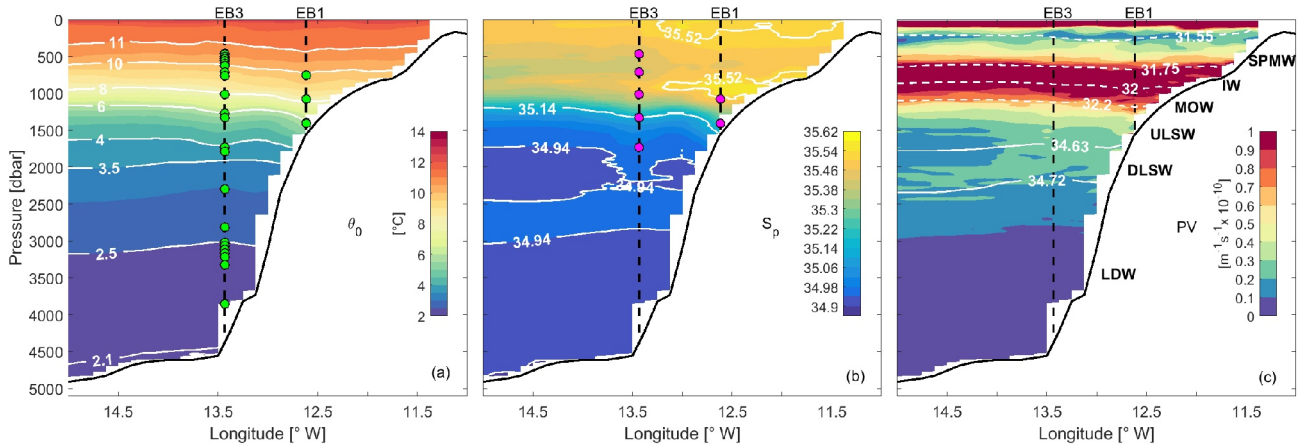

Figure 2. Composite sections of (a) potential temperature θ_0, (b) practical salinity S_P, and (c) potential vorticity (*PV*) obtained from four CTD surveys conducted during cruises MSM53 (2016), MSM64 (2017), MSM73 (2018), and MSM83 (2019). For the purpose of presenting, *PV* profiles have been vertically smoothed with a moving average filter using a width of 100 dbar. Vertical dashed lines indicate the positions of moorings EB1 and EB3. The white contour lines show (a) isotherms and (b) isohalines. Solid white contour lines in (c) indicate the $\sigma_{1.5}$-isopycnals, the dashed white contour lines indicate the σ_1-isopycnals. SPMW, subpolar mode water; IW, intermediate water; MOW, Mediterranean outflow water; ULSW, upper Labrador sea water; DLSW, deep Labrador sea water; LDW, lower deep water. The green circles in (a) depict the positions of moored temperature sensors. The magenta circles in (b) mark the positions of moored conductivity sensors. Section plots of the individual cruises are shown in the appendix (Figure B1).

Below the MOW lies a layer that is marked by contributions of LSW that originates in the Labrador Sea in the northwestern subpolar gyre. It enters the eastern basin by crossing the Mid-Atlantic Ridge (e.g., Rhein et al., 2015; Sy et al., 1997; Talley & McCartney, 1982). The layer is separated into an upper and a deep LSW mode (ULSW and DLSW, respectively), reflecting its temporally varying formation history (e.g., Kieke et al., 2009), and can be identified by a local *PV* minimum (Talley & McCartney, 1982). The freshest and thickest traces of both, ULSW and DLSW, are observed offshore from the slope region to the west of mooring EB3.

The deep to bottom part of the water column is formed of a thick layer of Lower Deep Water (LDW). It occupies about the lower half of the water column at water depths >2,000 m and is generally temperature-stratified, with colder and fresher water at depth, a salinity minimum close the bottom and an overall rather low PV (van Aken, 2000).

Table 2
Mean Depth Range of Water Masses Between mooring Positions EB1 and EB3 Obtained From CTD Sections of Cruises MSM53 (04/2016), MSM64 (06/2017), MSM73 (04/2018), and MSM83 (05/2019)

Watermass	Density range (kg m^{-3})	Depth range (m)
SPMW	σ_1 = 31.55–31.75	250–650
IW	σ_1 = 31.75–32.00	650–900
MOW	σ_1 = 32.00–32.20	900–1,150
ULSW	σ_1 = 32.20–$\sigma_{1.5}$ = 34.63	1,150–1,700
DLSW	$\sigma_{1.5}$ = 34.63–34.72	1,700–2,150
LDW	> $\sigma_{1.5}$ = 34.72	2,150–bottom

Note. Potential density ranges are listed relative to 1,000 (σ_1) and 1,500 ($\sigma_{1.5}$) dbar.
SPMW, subpolar mode water; IW, intermediate water; MOW, Mediterranean outflow water; ULSW, upper Labrador sea water; DLSW, deep Labrador sea water; LDW = lower deep water.

Figure 3 shows the composite flow field structure along the crest of Goban Spur as obtained from the repeated LADCP sections carried out annually during 2016–2019 (see Appendix, Figure B2, for individual sections). The velocity composites in Figure 3 represent spring-time conditions, as all involved cruises were conducted between early April and early June of the respective years (see Table 1). In both the along- and cross-slope components, the water column is composed of several current cores with alternating directions that often extend from the surface to the sea bottom. The along-slope component of the flow field (Figure 3a) shows the presence of the northbound shelf edge current (SEC) and Undercurrent (UC) in the shallow part of the continental slope (<1,000 m). Respective velocities are on the order of 4–6 cm s^{-1}. Mooring EB1 is installed to the west of the UC. There, the UC connects to the northbound deep eastern boundary current (deep EBC), which extends to about 13°30′W. The slope region between the 1,500 and 4,500 m isobaths, however, reveals counter-flows of moderate strength in the bottom part of the water column, which could be identified in three out of four individual LADCP sections (cf. Figure B2). We address this feature as the southbound counter current (CC). Mooring EB3 is located at the western edge of the deep EBC. Further offshore, the current changes direction, and a southbound flow

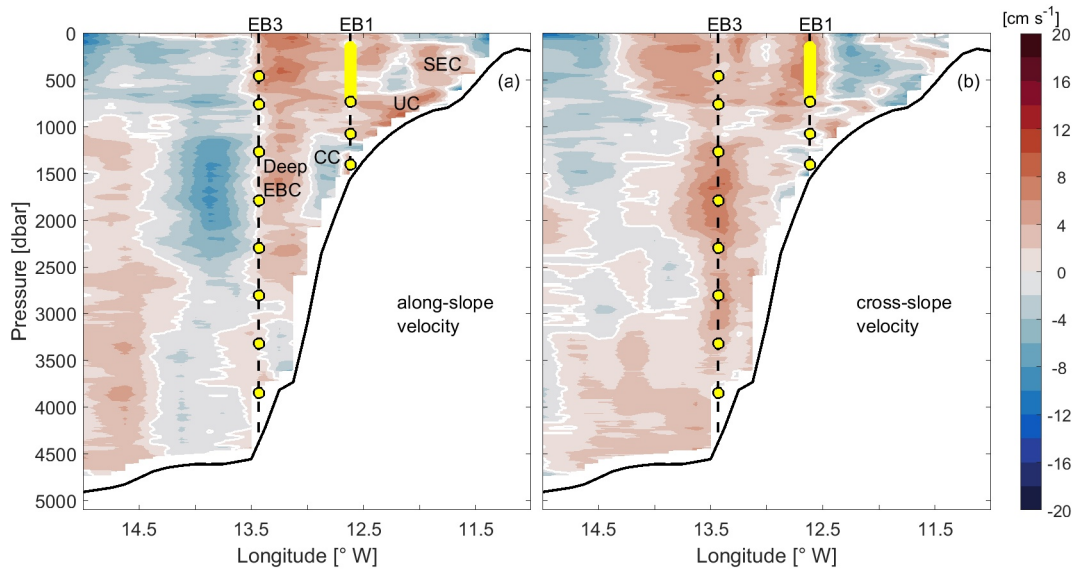

Figure 3. Composite section of de-tided (a) along-slope and (b) cross-slope velocity components obtained from four Acoustic Doppler Current Profiler (ADCP) surveys conducted during cruises MSM53 (2016), MSM64 (2017), MSM73 (2018), and MSM83 (2019). White contour lines indicate zero velocity. Vertical dashed lines show the positions of moorings EB1 and EB3. The yellow circles in (a) and (b) depict the position of moored single-point current meters. The range of the Longranger Acoustic Doppler Current Profiler (LR-ADCP) is highlighted by an yellow line. The terminology of the current system used in this study is added: SEC, shelf edge current; UC, undercurrent; CC, counter current; deep EBC, deep branch of the eastern boundary current. Reddish colors denote flow to the northwest (along-slope component) and toward the continental shelf (cross-slope component).

extending from the top to the sea bottom appears. Its maximum southward velocity of 9 cm s^{-1} is found between about 1,200 and 2,500 m in the LSW layer. The flow in the lower part of the water column is weaker with velocities below 5 cm s^{-1}.

The along-slope component in the EB region of the eastern Atlantic at Goban Spur shown in Figure 3 is of similar magnitude as the cross-slope component. Regarding the latter, most of the flow is directed toward the continental slope. The shallow part of the continental slope ($z < 1{,}000$ m) exhibits patches of onshore and offshore flow which is a common feature and present in all four individual sections (Figure B2). The western end of the composite section reveals offshore flow in the upper 1,500 m range of the water column, a feature that is observed in three of the four individual sections (cf. Figure B2). This is in contrast to conditions at the western boundary of the North Atlantic, where the meridional or along-slope component clearly dominates the flow field (e.g., Mertens et al., 2014; Zantopp et al., 2017), and cross-slope variations are much smaller compared to the mean flow.

4. Mean Flow and Current Variability Obtained From Moorings

The velocity field obtained from repeated LADCP sections provides insight into the larger-scale spatial current structure at the cost of limited information about temporal variability. The mooring records, however, though limited in space, allow to describe the long-term evolution of the current field. Current velocities recorded at the onshore mooring EB1 during April 2016 to May 2019 showed prevalent periods of strong, stable flow to the northwest at all sampled depths (Figure 4a) with maximum velocities of about 10–20 cm s^{-1}. These conditions are pronounced from July to December in all years and occurred additionally in April 2019. The flow was roughly barotropic, that is, periods of strong and weak flow were mostly consistent within the water column. There are exceptions, as in March 2018, where at 1,350 dbar maximum velocities of more than 10 cm s^{-1} directed northwestward were present, while the flow in the water column above was weaker or even directed southwards. From January–July 2017 and January to July 2018, the flow was weak

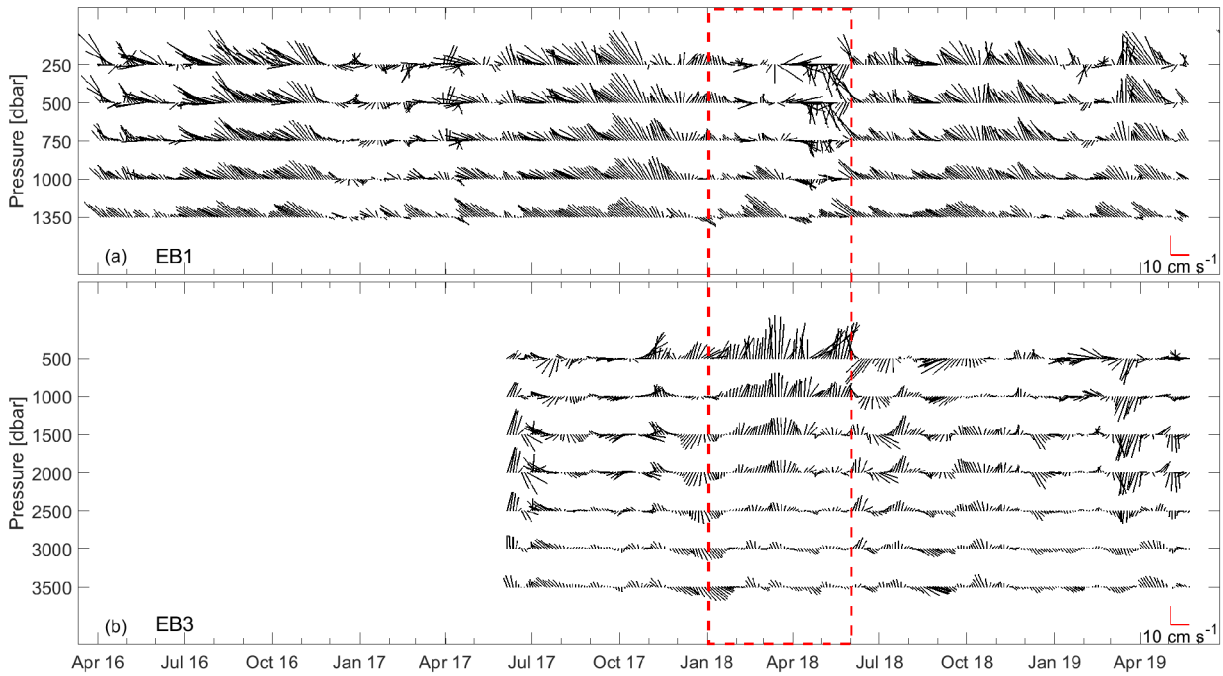

Figure 4. Stick plots of 10-day low-pass filtered velocity time series (a) at the onshore mooring EB1 from April 2016 to May 2019 (1,145 days) and (b) at the offshore mooring EB3 from June 2017 to May 2019 (718 days). The red box indicates the time slot from January to May 2018 discussed in the text. Shown is one stick per three days. Reference vectors are shown in the lower right corner of each plot. The upper three time series shown in (a) are selected records obtained from the Longranger Acoustic Doppler Current Profiler (LR-ADCP). All other time series denote single-point measurements. The *y*-axis indicates the instrument/record level of each time series. Upright sticks represent flow toward true north.

and more variable including flow reversals. During such unstable periods, the velocity vectors tended to rotate, which is indicative of the presence of eddies.

The situation at the offshore mooring site EB3 is very different from that at mooring EB1, that is, there was no signal of a persistent poleward boundary current in the period June 2017–May 2019 (Figure 4b). Instead, the flow was more variable with phases of offshore (southwestward and westward) and onshore (northward) flow accompanied by flow reversals and rotations of current vectors. Throughout the water column the variability differed, even though for some periods the flow was of barotropic character (e.g., March 2019). At times the variability was only partly coherent within the water column, for example, in January 2018 when below 1,000 dbar the flow was directed southward while it was directed northward above.

The period between January and May 2018 draws particular attention (red box in Figure 4). From February to April 2018, the current vectors at EB1 first rotated counter clockwise (CCW), then rotated clockwise (CW) over several weeks. During April 2018 the flow in the upper water column (250–750 dbar) turned southward and strengthened. In the following June, the flow again changed its direction and continued its northward progression. This behavior was less pronounced with increasing depth. At mooring EB3 the currents at 500 dbar alternated between periods of westward and northward direction. Looping patterns were present, for example, a CCW rotation during autumn and winter 2018/2019. This holds also for the flow at 1,500 dbar. Velocities at 3,500 dbar were generally weak and characterized by frequent flow reversals.

Figure 5 reveals the preferred flow direction at different depths at both mooring sites over the length of each velocity time series. The mean flow direction and maximum variance at the onshore mooring EB1 (Figure 5, right column) are oriented along the topography, that is northwestward. The mean speed is in the range of 5–6 cm s^{-1} throughout the observed depths. The orientation of the mean flow is 312° (clockwise relative to true north, T) at 250 dbar and 309° at 1,350 dbar. The angle of maximum variance (ψ) is negative at all pressure levels indicating a preferred clockwise rotation. The orientation of the major axis of the current ellipses along the mean flow direction indicates a pulsating (strengthening and weakening) character of the flow. The more circular shape of the current ellipses at 250–500 dbar reveals dominant isotropic motions at

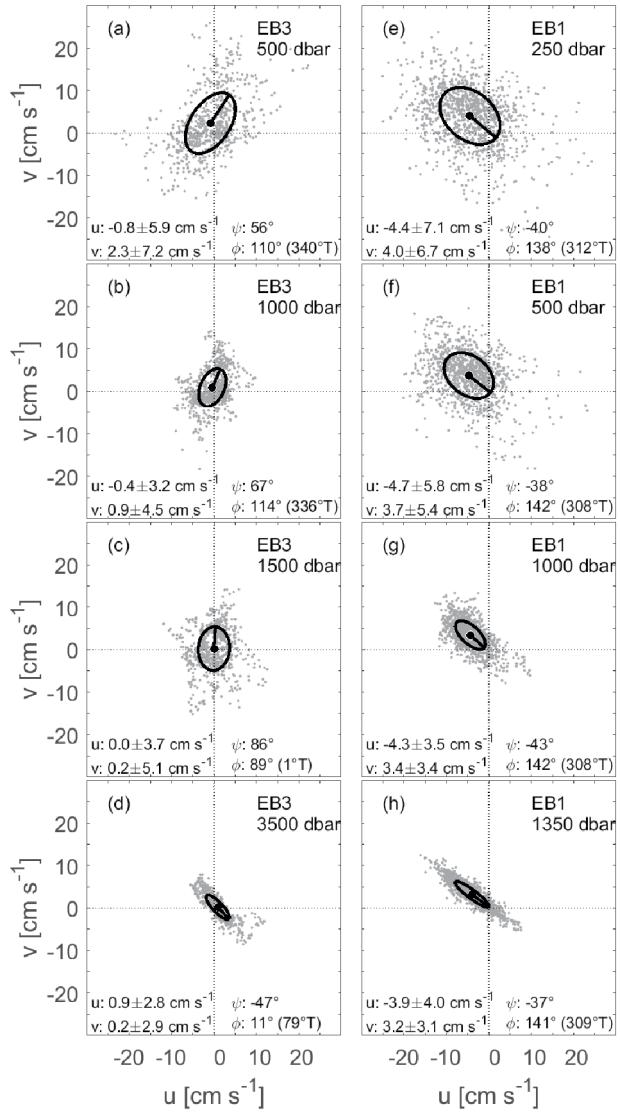

Figure 5. Scatter plots of daily velocity measurements for eastward and northward velocity components observed at mooring EB3 (left column) and mooring EB1 (right column). The EB3 records are shown for the pressure levels (a) 500 dbar, (b) 1,000 dbar, (c) 1,500 dbar, and (d) 3,500 dbar from June 2017 to May 2019 (718 days). The EB1 records are presented for the pressure levels (e) 250 dbar, (f) 500 dbar, (g) 1,000 dbar and (h) 1,350 dbar from April 2016 to May 2019 (1,145 days). The standard deviation ellipse is shown with the major axis indicated by the black solid line and the mean velocity by the black dot. Mean and standard deviation of the velocity components are given in the lower left of each subplot. The angle ψ is the angle (or direction) of maximum variance relative to the x-axis (east). Hence, $\psi > 0$ indicates counter-clockwise and $\psi < 0$ clockwise rotation. The angle ϕ is the angle of the mean flow direction counter-clockwise relative to the x-axis (east) and clockwise relative to true North (°T). Note the different pressure levels shown for the moorings.

250–500 dbar changing to an-isotropic motion toward the bottom, where the ellipses are elongated. Cross-slope variance decreases from top to bottom, as the flow becomes more confined by topography in its lateral extension with increasing depth.

The mean flow at mooring EB3 is weak with a mean speed of about 2 cm s^{-1} at 500 dbar and about 1 cm s^{-1} and less at larger depths (Figure 5, left column). The variability is strong with a standard deviation of about 3–7 cm s^{-1}. At EB3, the variance ellipses change their orientation with depth. At 500–1,500 dbar, the flow is dominantly varying in north/northeast and south/southwest direction, that is cross-slope. The major axis of the current ellipse at 500 and 1,000 dbar is oriented 54° and 47° relative to the mean flow direction implying a meandering character of the flow. At 1,500 dbar, maximum variance is oriented along the north-south axis. At 3,500 dbar, the variance ellipse is tighter indicating an-isotropic flow that is oriented along the topography. The angle ψ is positive for 500, 1,000, and 1,500 dbar revealing preferred counterclockwise rotation, while at 3,500 dbar, it is negative indicating a preferred clockwise rotation.

In order to obtain along-slope and cross-slope velocity components of the flow field, we rotated the horizontal velocity vectors of all time series clockwise by 48°. This angle of rotation was obtained from the above analysis of velocity time series at EB1 and EB3 assuming that the current ellipses of the near-bottom flow are oriented along the topography. In particular, we took the absolute mean value of the angle ψ obtained for the two bottom-near velocity time series at moorings EB1 and EB3 (Figures 5d and 5h) and subtracted it from 90°. The same angle-rotation was applied to the previously presented LADCP data, as already stated in Section 2.2.

4.1. Spectral Analysis of Along- and Cross-Slope Velocity Time Series

For the spectral analysis of the time series, we use the multitaper method (MTM) that allows for spectral estimation and signal reconstruction using a set of orthogonal tapers or windows (Percival & Walden, 1993; Thomson, 1982). The version used here is the one implemented in the MATLAB toolbox of Lilly (2019). By using a small set of tapers rather than a unique spectral window or data taper as is the case in other methods, the MTM approach reduces the variance of spectral estimates. A crucial parameter that has to be set in the MTM is the time-bandwidth product NW, where N is the number of sample points and W is the bandwidth. The number of tapers k used to compute the spectrum is $k = 2NW - 1$. As NW increases, there are more realizations of the power spectrum, and the variance of the estimate decreases. Also, as NW increases, each estimate exhibits more spectral leakage (i.e., wider peaks) and the overall spectral estimate is more biased. In other words, a larger choice of NW gives a smoother result, but the spectral peaks are smeared out at low frequencies.

NW was chosen here by starting with a small value and then increasing iteratively to find an optimum trade-off between frequency bias and variance. We chose $NW = 8$ ($k = 15$) for velocity records obtained at EB1 and $NW = 5$ ($k = 9$) velocity records at EB3. Thus, the bandwidth W for the time series of mooring EB1 with $N = 1{,}145$ days and mooring EB3 with $N = 718$ days is $7 \cdot 10^{-3}$ day^{-1}, that is, the inverse of a period range of 143 days. Confidence intervals (CI) at

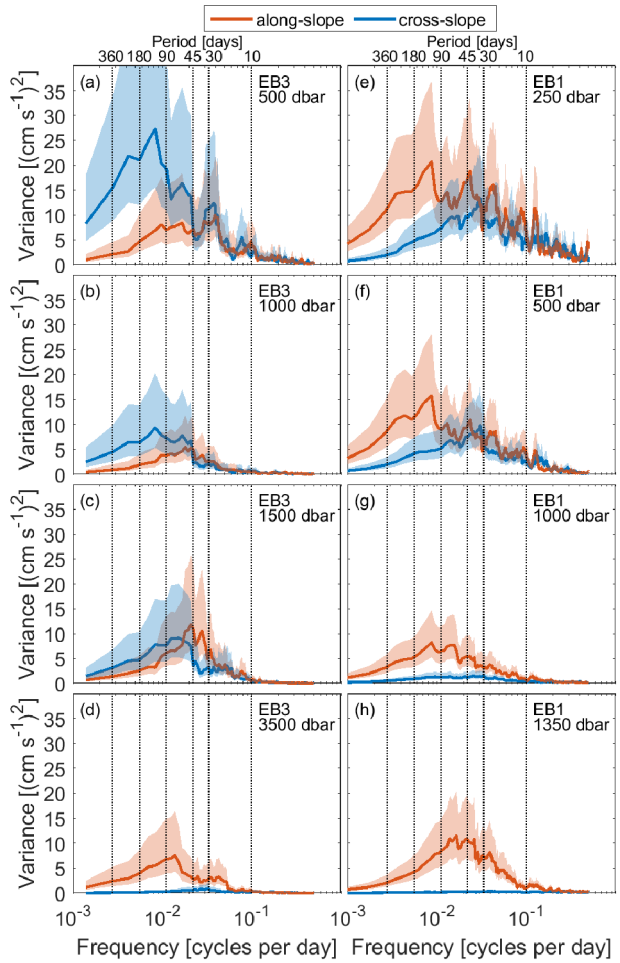

Figure 6. Variance-preserving power spectra of along-slope (red) and cross-slope (blue) velocity components for mooring EB3 (left column) and mooring EB1 (right column). The EB3 spectra ($k = 9$ tapers, $N = 718$ days, bandwidth $W = 1/143$ days^{-1}) are presented for the pressure levels (a) 500 dbar, (b) 1,000 dbar, (c) 1,500 dbar, and (d) 3,500 dbar for the period June 2017–May 2019. The EB1 spectra ($k = 15$ tapers, $N = 1{,}145$ days, bandwidth $W = 1/143$ days^{-1}) are shown for the pressure levels (e) 250 dbar, (f) 500 dbar, (g) 1,000 dbar, and (h) 1,350 dbar for the period April 2016–May 2019. Shaded areas indicate the 95% confidence intervals. Individual periods of interest are highlighted by dashed vertical lines and labeled at the top of each column. Note the different vertical levels for each of the moorings.

the 95% level are estimated from a χ^2 distribution. A higher number of tapers results in narrower CIs, but in less variance.

Figure 6 presents the variance-preserving power spectra for the same depth levels of moorings EB1 and EB3 as displayed in Figure 5. Velocity variance at the onshore mooring site EB1 is generally dominated by the along-slope component (Figure 6, right column). In the upper water column (250 dbar; Figure 6e) we find distinct spectral peaks in this component at about 42 and 115 days. On weekly time scales, the spectrum shows peaks at 23, 17, 11, and 8 days. The variance at high frequencies diminishes with increasing depth, but also the variance at low frequencies (the peak at 115 days) is reduced at larger depths (Figures 6f–6h). In the deep part of the water column, the variance peaks in the period band 30–90 days.

Notable spectral energy in the cross-slope component at mooring site EB1 is only present in the upper part of the water column (250 and 500 dbar, Figures 6e and 6f). There, spectral energy on monthly and shorter time scales is at a comparable level as in the along-slope component. On longer than monthly time scales, variance in the cross-slope component is considerably reduced and does not show any noticeable peak beyond 90 days. At the deeper levels (1,000 dbar and 1,350 dbar), spectral energy in the cross-slope component is only slightly elevated at time scales ranging from 10 to 180 days (1,000 dbar level) and almost nonexistent at 1,350 dbar.

The spectral energy distribution at the offshore mooring site EB3 shown in Figure 6 (left column) gives a very different impression. At periods shorter than 45–30 days, variance in both, along- and cross-slope components, is of similar magnitude. At longer periods, the variance in the upper and intermediate water column is dominated by the cross-slope component. With increasing depth, the energy of the cross-slope variation diminishes. The amplitudes of the along-slope and cross-slope variance are of similar order (10 cm^2 s^{-2}) at 1,500 dbar (Figure 6c), which corresponds to the approximate depth of the ULSW layer, and still elevated in a period band ranging from 30 to 90 days. Near the bottom, the along-slope variations clearly dominate over cross-slope variations, as is the case for mooring EB1.

Similarities in the spectral energy distribution between EB1 and EB3 are found in the upper layer (<=500 dbar). At shorter time scales, the velocity variance shows peaks of energy at periods of about 11 days in the upper layer at both moorings. Energy peaks are found at both EB1 and EB3 at about 23–27 days and 115–120 days, but in different velocity components. The peak at 42 days seen in the spectrum of the onshore mooring EB1 is absent at the offshore mooring EB3. In the ULSW layer (Figures 6c and 6h) the spectrum of the along-slope component exhibits a band of high energy in the period range between 30 and 90 days and centered at 45 days. Due to the limited duration of our mooring records and our choice of a bandwidth corresponding to a period range of 143 days, seasonal time scales are not sufficiently resolved in the spectral analysis. All spectra thus flatten toward the low-frequency range.

4.2. Variability of the Upper Flow Field on Monthly to Seasonal Time Scales

The spectral analysis for the mooring period April 2016–May 2019 revealed high spectral energy for periods exceeding 10 days, thus in the monthly range, as well as for periods longer than 90 days in the subseasonal

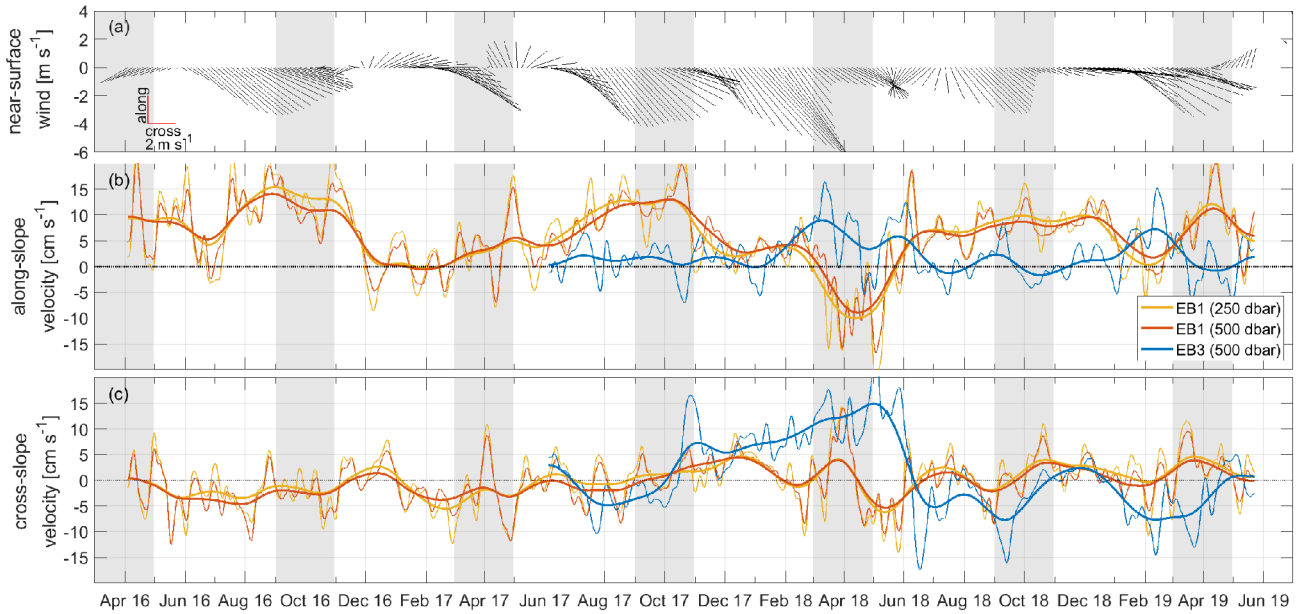

Figure 7. Time series of (a) 90-day low-pass filtered near-surface wind vectors from the ERA5 reanalysis, (b) cross-slope, and (c) along-slope velocity components for EB1 at 250 dbar (yellow) and 500 dbar (red) and EB3 at 500 dbar (blue). Thin (thick) lines in (b) and (c) are 10-day (90-day) low-pass filtered time series. In (a), one stick per 5 days is shown. The shaded gray areas indicate the months of the SOMA pattern (September-October and March-April; e.g., Pingree et al., 1999).

to seasonal range (Figure 6). A known feature of wind-forced variability in the region of interest is the so-called SOMA response. This feature is characterized by a stronger poleward flow in September-October (SO) and reduced or even reversed (equatorward) flow during March-April (MA) seen on the shelf part of the ESC (Huthnance et al., 2001; Pingree & Le Cann, 1989, 1990; Pingree et al., 1999; Xu et al., 2015). Using a 90-day low-pass filter, we now focus on these frequency bands, while removing much of the typically prevailing short term variability of the wind. We thus compare the filtered velocity time series recorded at the mooring sites in the upper part of the water column with the wind field obtained from the ERA5 reanalysis.

The EB1 time series denoting the along- and cross-slope flow at the 250 and 500 dbar levels are very similar in both strength and variability (Figure 7). This stresses the previously noted rather barotropic nature of the flow field at mooring site EB1. It is, however, different from the shallowest EB3 time series (500 dbar). There, the along-slope component is in general much weaker and in early spring 2018 and 2019 partly out of phase with the along-slope component at EB1. Comparing the currents at moorings EB1 and EB3 during the overlapping observation period, we find negative correlations for the 90-day low-pass filtered time series at 500 dbar ($r = -0.7$ for along-slope velocities at EB1 and cross-slope velocities at EB3; $r = -0.6$ for along-slope velocities at both moorings), indicating a phase shift of about 90° on monthly to seasonal time scales between the two moorings (Figure 7). At time scales of 10 days and longer, the relationship is less strong ($r \approx -0.4$). Direction changes of the flow can occur abruptly. For example, the cross-shelf component at EB3 increases and is directed on-slope (positive) for several months during autumn 2017–spring 2018, then within 2 weeks it decreases rapidly and the flow turns off slope (negative).

The atmosphere over the region of interest was dominated throughout the mooring period by westerly winds (Figure 7a). During our observation period, these winds were often strongest in late summer to early fall and weaker in late spring to early summer. The winter 2018/2019 showed a number of successive months with rather low wind speeds. However, over this 3-year period we do not see a clear SOMA-response pattern in the wind field, even when allowing variability in the timing of the phases of ±1–2 months. Strengthening or weakening of the wind often started before or extended beyond the SO- or MA-phases. Early spring 2018 (March–May) reveals the only period with a prevalent reversed flow (i.e., equatorward) at the EB1 mooring site. This would correspond to the weakening phase of the SOMA pattern and happens at a time of reduced wind strength. The preceding late summer to fall period 2017 shows the opposite, that is, a strengthening of

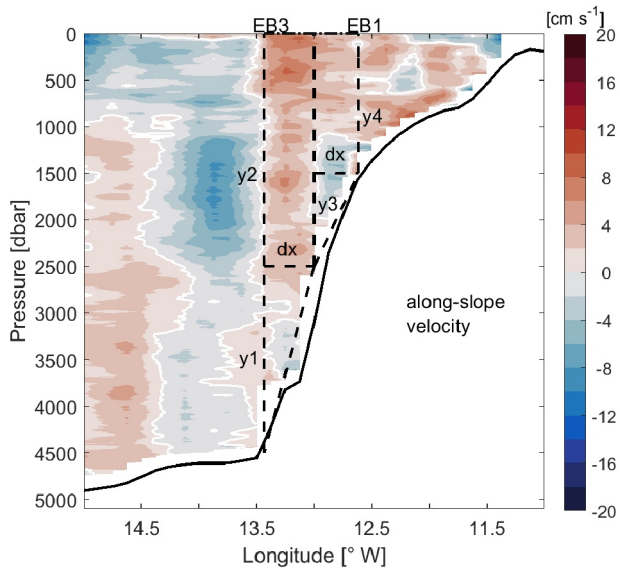

Figure 8. Integration limits for estimating the volume transport of the deep eastern boundary current (EBC) based on ship-based velocity measurements shown in Figure 3a. Dashed black lines show the area used for transport calculations as described in Section 4.3. See text for a description of dx_i and y_i distances.

the poleward flow at site EB1 that coincides with a strengthening phase of the SOMA wind pattern but starts already in summer. The along-slope component at the EB3 site does not show any resemblance to the SOMA pattern. On the contrary, poleward flow at EB3 is strengthened in early spring 2018, which is in contrast to the flow direction suggested for such a SOMA-phase. While in the upper flow field at the EB1 site indications of a SOMA-like pattern in the period fall 2017 to spring 2018 are found, the EB3 record does not reveal such kind of variability.

4.3. Volume Transport Time Series of the Deep EBC

The analysis of the ship-based and mooring-derived velocity distribution and time series (e.g., Figures 3, 4 and 7) so far revealed that there is a considerable poleward flow in the Goban Spur region at the locations of the moorings EB1 and EB3. This is stronger and more prominent at the shallower onshore mooring site EB1 and more intermittent and weak at the deeper offshore mooring site EB3. In order to quantify the overall strength of this poleward flow, we now infer time series of along-slope volume transports. These transports can be interpreted as the contribution of the deep EBC to the entire ESC system at Goban Spur (see Figures 1 and 3). Assumptions and uncertainties of our approach are discussed below. Since the EB3 mooring record is shorter by about 1 year, we focus on the common mooring period ranging from June 2017 to May 2019.

4.3.1. Mooring-Derived Transports, 2017–2019

The horizontal and vertical integration limits to infer the area for transport calculations are schematically shown in Figure 8. First, we vertically average the 10-day low pass-filtered time series of the along-slope current velocities from top to bottom at each mooring site. In order to account for the transport in the near-surface layer that is not resolved by the moorings, we choose the following simplistic approach. The LADCP measurements (Figure 3) as well as the mooring records (Figure 4) suggest a barotropic structure of the upper water column. We thus assume the uppermost velocity value at each mooring (250 m for EB1, 500 m for EB3 after vertical interpolation) to be representative for the upper water column. The same approach is applied for obtaining the bottom-near transport, that is, we assume the deepest measured velocity record of each mooring to be representative for the bottom-near part of the water column. This corresponds to assuming a barotropic velocity structure in the lower 100 m (650 m) of the water column for EB1 (EB3). Then, we multiply them with an area that is assumed to be representative of the local current structure. The current system cannot be fully resolved with data from only the two available moorings. Thus, assumptions have to be made about the spatial structure of the flow. The horizontal spacing between the moorings is 62 km, so each mooring is weighted with half of this distance, that is, 31 km. This scale is larger than the local first baroclinic Rossby radius of deformation that is 10–20 km in this region (Chelton et al., 1998). To avoid extending the horizontal scaling too far outside of the domain, we stick to this rather conservative approach to obtain the volume fluxes. Even if we extend the area needed for calculating the transports outside of the mooring domain, it would only affect the magnitude of the volume transport but not its variability.

The volume transport V representing the strength of the deep EBC at Goban Spur is calculated by a simple geometrical approach, as indicated in Figure 8:

$$V_{EB1} = \overline{v}_{EB1}\left(\frac{1}{2}y_3 + y_4\right)dx \tag{1a}$$

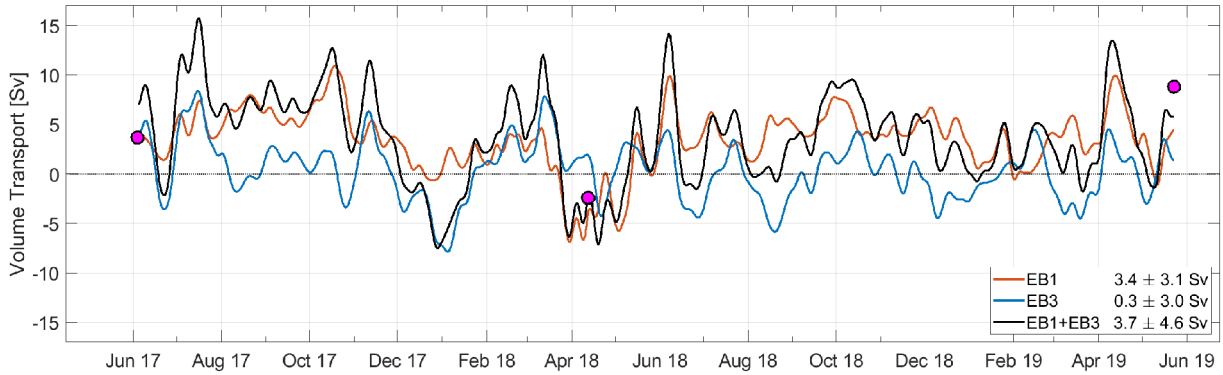

Figure 9. Volume transport time series for the period June 2017 to May 2019 from 10-day low-pass filtered along-slope velocity time series, integrated from top to bottom (EB1: 0–1,500 dbar; EB3: 0–4,500 dbar). Transports are estimated for EB1 (red), EB3 (blue) and both combined (black). Mean values and standard deviations are given in the lower right corner. Magenta dots indicate volume transports derived from Lowered Acoustic Doppler Current Profiler (LADCP) sections obtained during the ship surveys. See Section 4.3.2 for a discussion of errors.

$$V_{EB3} = \overline{v}_{EB3}\left(\frac{1}{2}y_1 + y_2\right)dx \tag{1b}$$

where $\overline{v}$ is the vertically averaged along-slope velocity, $dx = 31\,km$, $y_1 = 2000\,m$, $y_2 = 2500\,m$, $y_3 = 1000\,m$, and $y_4 = 1500\,m$. The total area for EB1 and EB3 is $62.0 \cdot 10^6$ m^2 and $108.5 \cdot 10^6$ m^2, respectively. The total transport of the deep EBC captured by the moorings is then $V = V_{EB1} + V_{EB3}$.

Figure 9 shows the resulting along-slope transport time series for the deep EBC in the period June 2017–May 2019 inferred from both moorings separately and for the sum of both. The mean and standard deviation of the total volume transport over this period is 3.7 ± 4.6 Sv ($1\ \text{Sv} = 10^6\ m^3\ s^{-1}$). The standard error of the mean, obtained from a decorrelation time scale of 15 days, is 0.7 Sv. The total transport is thus poleward on average, but periods of equatorward transport occur. Transport values range from −7.5 to 15.7 Sv and can change rather abruptly, that is, decrease or increase by more than 10 Sv within less than a month. We find two strong equatorward volume flux events in the time series exceeding −5 Sv, which occurred in winter 2017/18 (December, January) and spring 2018 (April, May), see black line in Figure 9. The LADCP-derived transport estimates either match the mooring-based time series or support the general tendency of a positive or negative transport phase.

Considering the contributions of each mooring site separately, the transport at EB1 is predominantly positive (i.e., poleward) and 3.4 Sv in the mean, while at EB3 it oscillates around zero with 0.3 Sv on average. The standard deviation is about 3 Sv and similar for both mooring sites. Spectral energy of the deep EBC transport time series (not shown) peaks at similar periods as the along-slope velocity in the upper water column at EB1 and is most pronounced at 120 days and near 30 and 20 days.

The individual contributions of individual water masses to the deep EBC transport according to Table 2 are summarized in the appendix in Table D1.

4.3.2. Assessment of Transport Uncertainties

Uncertainties in the transport estimates arise from various sources. The overall error due to individual instrument uncertainty is 0.24 Sv, derived from the error of the daily velocity averages. The lack of velocity measurements close to the surface may lead to a potential bias toward lower transports as near-surface currents are expected to be stronger and more variable due to wind forcing. Thus, our approach to infer the top-to-bottom volume transport of the deep EBC could underestimate the actual transport and its variability. Since we use 10-day lowpass-filtered data, any effects from short-scale wind bursts are, however, not relevant. We thus consider this bias to be low. In contrast, the observed velocity field obtained from the LADCP observations indicates near-bottom counter-currents next to the continental slope (Figure 3a), which might be missed by the spacing and positioning of our moorings on the slope. As a consequence, there would be an overestimation of the mooring-derived poleward transport. However, these currents are not likely to be

stationary, but rather shift their position on the slope and thus are partly covered by the measurements. Furthermore, we cannot conclude from the snapshots of the ship section if those currents are permanent throughout a year. The velocity time series of the deepest current meter at mooring site EB1 (1,350 dbar, Figure 4) showed very few occasions of an equatorward flow that started and ended rather abruptly. These short-term events might have been caused by an equatorward counter-current that occasionally shifted higher up the slope and could thus be captured by the bottom-near EB1 current meter.

The LADCP composite (Figure 3) allows us to estimate the transport uncertainty that arises from assuming uniform velocities above (below) the shallowest (deepest) mooring records, and we find a transport reduction of 0.4 Sv due to this assumption. In addition, the LADCP composite suggests that the moorings EB1 and EB3 are located at the edge of rather narrow current branches. Mooring EB3 is located close to the transition zone from positive flow to negative flow in this velocity distribution, thus missing the northward current core. Again, this could bias our mooring-derived transports to lower values. We argue here as well that these current cores are not likely to be stationary and should be covered by our moorings occasionally. The velocity distribution from LADCP measurements additionally represents only summer snapshots.

The LADCP measurements can furthermore be used as an independent comparison to our mooring-derived transport estimates. Data from the four ship surveys give an average transport of 3.7 Sv with a standard deviation of 4.6 Sv. Individual estimates range from −2.4 Sv (April 2018) to 8.8 Sv (May 2019). These estimates are well within the range of our mooring-derived estimates and agree in terms of mean and standard deviation (Figure 9). Applying the calculation method as outlined in Equations 1a and 1b to the vertically averaged LADCP velocities at the positions of EB1 and EB3 results in 0.6 Sv less transport compared to using the full LADCP data coverage.

4.3.3. Reconstruction of the Deep EBC Volume Transport for the Period 1993–2019

The mooring data set and ship surveys discussed so far represent the state of the deep EBC at Goban Spur for a limited time, but lack information on the long-term evolution. Several studies focusing on the circulation of the western boundary current and NAC in the western, central or eastern subpolar North Atlantic have successfully demonstrated the reconstruction of their volume transports, when combining shorter-term time series from moored devices with decadal records from satellite altimetry data (e.g., Rhein et al., 2019; Roessler et al., 2015;Nowitzki et al., 2021). Here, we take a similar approach to reconstruct the transport time series of the deep EBC by exploiting the gridded geostrophic surface velocities provided by CMEMS (see Section 2.4 for details). We thus perform a multilinear regression of the mooring based volume transport time series on the 10-day low-pass filtered altimeter-based surface geostrophic velocities at the grid points closest to our mooring positions. In particular, we use the u and v components of the surface geostrophic velocities at both grid points as predictors for the regression in order to reconstruct the long-term deep EBC volume transport time series.

For the overlapping mooring period (2017–2019), we find a significant correlation ($r > 0.7$) between the 10-day low-passed surface geostrophic velocities derived from the altimeter observations and vertical velocity averages in the 500–1,000 dbar range of the water column. Comparing the surface geostrophic velocities with vertical velocity averages from top to bottom, we still find a good correlation for EB1 ($r \approx 0.7$), but a weaker correlation ($r < 0.4$) for EB3 due to the more baroclinic character of the deep EBC at this location. All correlations are significant at $p < 0.05$.

Figure 10 compares the mooring-derived transport time series for the deep EBC to those reconstructed from the altimeter-derived surface geostrophic velocities. The regression model explains 66% of the transport variance with a root mean square error (RMSE) of 1.8 Sv at mooring site EB1. For data from mooring site EB3, the model is less effective, capturing only 22% of the transport variance with an RMSE of 2.6 Sv. However, for the total transport, that is, the sum of transports at EB1 and EB3, the model fits the mooring-derived observation well, explaining 52% of the variance with a RMSE of 3.1 Sv and a significant correlation with $r \sim 0.7$. The reconstructed time series of the total transport captures the general changes, even though the RMSE is as high as the mean. Most of the error results from mooring EB3, while the transport is dominated by mooring EB1.

As was the case for other regions in the subpolar North Atlantic (e.g., Rhein et al., 2019; Roessler et al., 2015; Nowitzki et al., 2021), the results from the regression model applied to data from the Goban Spur explain

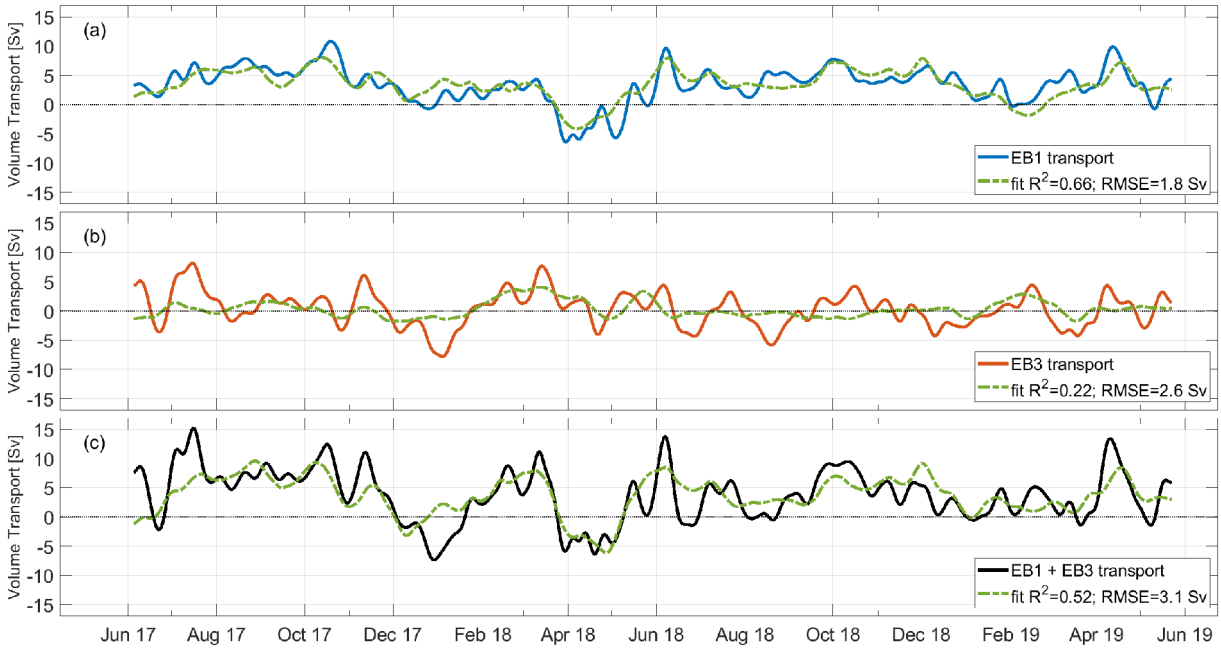

Figure 10. Time series of the 10-day lowpass filtered volume transport of the deep eastern boundary current (EBC) at (a) mooring EB1 (blue), (b) mooring EB3 (red), and (c) the sum of EB1 and EB3 (black) from moored observations and derived from a multilinear regression (green) of the mooring-based transport on altimeter-derived surface geostrophic velocities during June 2017–May 2019. The R^2 statistics and root mean square error (RMSE) for each fit are indicated in the lower right of each subplot.

a high amount of the variance in the mooring-derived time series. This allows to take advantage of the full altimetry record covering the years 1993–2019, in order to reconstruct the volume transport of the deep EBC over this period. Due to the lack of suitable historical data, we cannot assess any change of the regression model for periods preceding our mooring observations. Consequently, we assume this regression to be valid for the entire altimetry period. The transport time series derived from this method covering the years 1993–2019 is depicted in Figure 11. The time series has been smoothed by applying a low-pass filter of 10 days in order to filter out variability on short time scales. In addition, we have added the same time series but with a 360-day low-pass filter applied to highlight interannual variability.

The long-term mean of the deep EBC volume transport time series (Figure 11) is 3.2 Sv with a standard error of the mean of 0.4 Sv, obtained from a de-correlation time scale of 89 days, and a standard deviation of 4.6 Sv. This result agrees well with our 3.7 Sv mean estimate for the short-term mooring period. The 10-day low-pass filtered time series reveals that transport amplitudes range from −11.5 Sv (July 2015) to +15.5 Sv

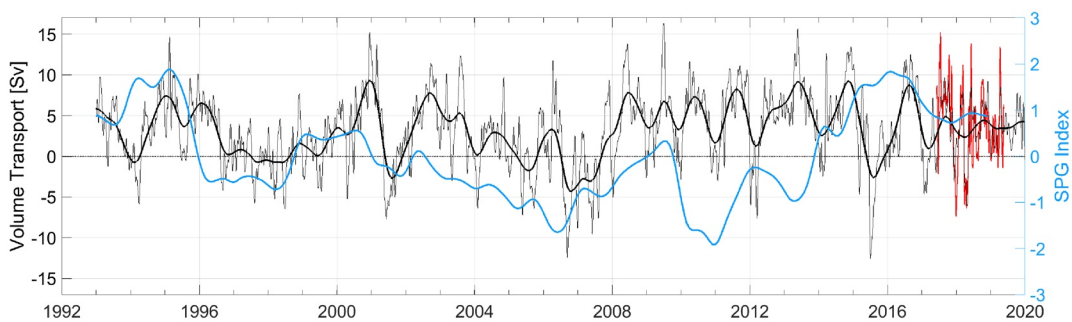

Figure 11. Time series of the deep eastern boundary current (EBC) volume transport obtained from a multilinear regression of the mooring-based transport on altimeter-derived surface geostrophic velocities, extended for the period from 1993 to 2019. Thin (thick) black lines are the 10-day (360-day) low-pass filtered estimates. The red line is the deep EBC transport time series obtained from both eastern boundary (EB) moorings as shown in Figures 9 and 10c. The blue line is the 12-month low-pass filtered time series of the monthly subpolar gyre (SPG) index (Chafik, 2019).

(July 2009) over the course of the time series. Nevertheless, poleward volume flux is the usual state of the deep EBC at the mooring locations, while strong short-term fluctuations with rapid flow reversals from poleward to equatorward flux and vice versa exist at times (e.g., years 2001, 2008/2009, 2012, 2015). For the time of the mooring period, both, mooring- and altimetry-derived transports, agree on the variability, though the altimeter record tends to smooth out some of the extremes (also compare Figure 10c). Short-term equatorward flow occurred more often before 2008, when the overall variability pattern of the deep EBC transport was different compared to later years, as can be seen best in the 360-day low-pass filtered time series. The late 1990s, for example, showed a rather weak deep EBC with average transports close to zero. In early 2001, there was a strong decrease in the transport from almost +10 Sv–−2 Sv that reached its minimum in mid-2001 and was followed by a rather steep increase to about 7.5 Sv. From 2002 to 2006/2007, there was a general long-term decrease of the deep EBC transport toward equatorward flow. This was superimposed on still existing short-term fluctuations on the order of ±10 Sv. During the period 2006–2008 transport levels generally increased to about +7 Sv. This increase was followed by a longer period with the poleward transport of the deep EBC more or less oscillating around 5–7 Sv (years 2008–2015). For the mooring period we note that the flow of the deep EBC during 2017–2019 does not represent any obvious anomalous state, that is, no prominent long-term increase or decrease. It rather remained oscillating at lower values than before (around 3 Sv).

From 1993 to 2019, the 10-day low-pass filtered time series has a positive linear trend of 2.0 ± 0.3 Sv that is significant at the 95% confidence level. This trend corresponds to an increase of 0.7 Sv per decade, which is in the same direction but smaller than the trend of 2.0 Sv per decade, reported by Nowitzki et al. (2021) for the meridional top-to-bottom flow across 47°/48°N in the region between ~31°W and 15°W. So, the trend in the eastern boundary current and the interior eastern North Atlantic opposes and within uncertainties balances the negative trend observed in the western basin (Nowitzki et al., 2021; Rhein et al., 2019).

Causes for low-frequency variability in our time series may be found in variability patterns of the regional current system, such as variations in the SPG strength (e.g., Häkkinen & Rhines, 2004, 2009). Included in Figure 11 is the index representing the strength of the SPG following Hátún and Chafik (2018) and Chafik (2019) (their second principal component, PC2). The SPG index indicates with negative (positive) values a weaker (stronger) than average surface circulation of the SPG. Over the length of the transport and SPG index time series (Figure 11), there are several longer periods when the evolution of the deep EBC transport seems to follow that of the SPG index, but from 2009 onward the behavior of the time series differs strongly. Especially the oscillating fluctuations of the deep EBC transport noted above do not find a similar expression in the SPG strength. The overall low agreement between SPG index time series and our deep EBC transports confirms the weak connectivity of the SPG strength with the circulation in the European shelf break region (Hátún and Chafik (2018), their Figure 1).

4.4. Impact of the Larger-Scale Circulation System on the Flow Field Observed at Goban Spur

In order to relate the variability in the mooring derived timeseries (e.g., Figures 4 and 9) to changes in large-scale circulation patterns, we now analyze mapped fields of Absolute Dynamic Topography (ADT). For this, we use the ADT fields and corresponding absolute geostrophic surface velocities of the CMEMS altimetry product (see Section 2.4).

Figure 12 presents spatial distributions of ADT and absolute geostrophic surface currents averaged over three different periods (long-term mean, mooring period, early 2018). The shortest averaging period (Figure 12c) represents the state of the circulation in the first 5 months of 2018, when we observed considerable changes in our mooring records compared to earlier and later times (see red frame in Figure 4). The spatial patterns are as expected more smooth (detailed) when averaging over the longest (shortest) period of interest.

The absolute geostrophic surface velocity field averaged on longer time scales (Figure 12a) and over the period June 2017–May 2019 (Figure 12b) does not reveal a persistent and well-expressed ESC system that originates somewhere in the Bay of Biscay and clearly propagates poleward along the continental margin. The surface pattern is rather complex, and poleward flow persist at mooring site EB1, which is different for site EB3. The most noticeable features are related to offshore current branches that originate from the NAC

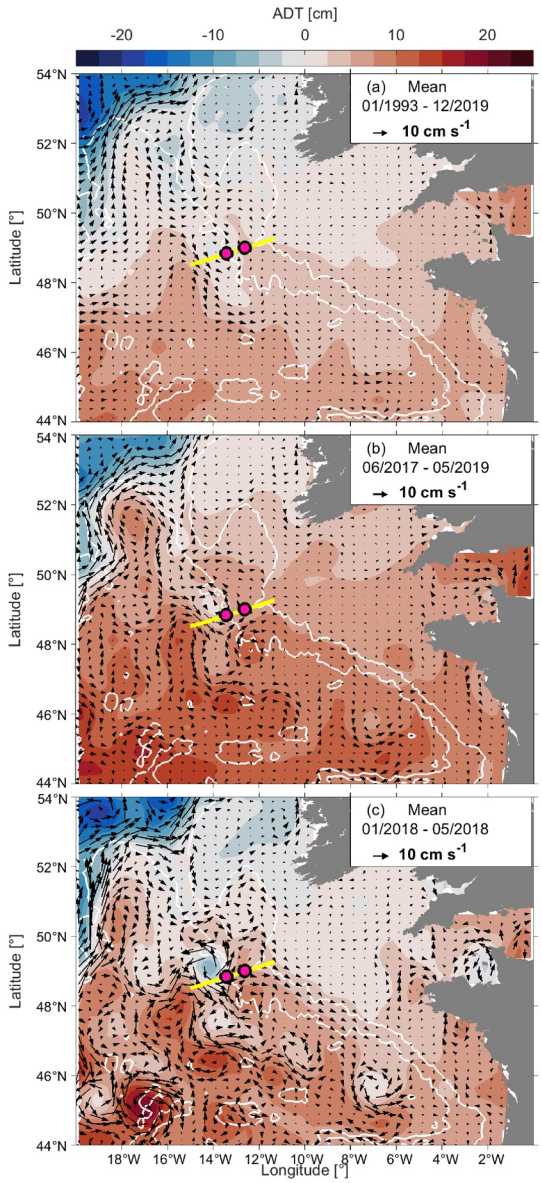

Figure 12. Maps of mean Absolute Dynamic Topography (ADT, colored contours) and absolute geostrophic velocities (black arrows) averaged for (a) the period from January 1993 to December 2019 (9,861 days), (b) the overlapping mooring period from June 2017 to May 2019 (718 days), and (c) the period January 2018 to May 2018 (thus covering the period highlighted in Figure 4). The positions of the moorings are indicated by magenta dots. The yellow line marks the cruise track for the hydrographic section shown in Figure 2. White contour lines indicate the 1,000 and 4,000 m isobaths.

and meander toward the mooring sites, thereby coming from the west or northwest. A distinct and persistent feature of the local circulation is the presence of a branch of the NAC in the northwestern corner of the region of interest, following the approximate course of the 4,000-m isobath. Originating in the western subpolar North Atlantic (e.g., Rossby, 1996; Mertens et al., 2014), the NAC first has to cross the Mid-Atlantic Ridge (e.g., Bower & von Appen, 2008; Roessler et al., 2015) before it approaches the eastern boundary of the North Atlantic and joins the ESC system near Porcupine Bank and the Rockall Trough. East of 16°W, the 4,000-m isobath bends and stretches along the continental slope. Thus, topography appears to redirect a branch of the NAC southeastward (Lherminier et al., 2010). In the vicinity of Goban Spur, this NAC-origin flow interacts with eddies and contributes further to the formation of vortices. A recently described NAC branch flowing into the eastern basin without making a detour via the subpolar western basin (Nowitzki et al., 2021; Stendardo et al., 2020) cannot be clearly identified from the maps shown here.

The flow over the slope region south of Goban Spur ($z < 4{,}000$ m) is particularly weak with varying direction (Figure 12a) or a tendency toward equator-ward flow (Figure 12b). This flow direction stands out even stronger and persists over larger scales when investigating the flow field during early 2018 (Figure 12c). This period shows a pronounced equator-ward flow stretching along the slope over the 4,000 m–<1,000 m depth range from Porcupine Bank in the north to the French shelf in the Bay of Biscay.

All three maps reveal a complex meandering of the current field in the vicinity of the mooring sites with the presence of meso-scale cyclonic and anti-cyclonic vortices. When analyzing the circulation fields in conjunction with eddies and their respective trajectories obtained from the Mesoscale Eddy Trajectory Atlas (META, cf. Section 2.4), we find that sizes and positions of such vortices are persistent on time scales from weeks to months. Over the period 1993 to 2019, we identify 232 eddies in the META data set that pass through a box defined by ±1° around the mooring location, corresponding to about 9 eddies per year. Out of these, 105 eddies are anti-cyclones and 127 are cyclones. The mean radius and lifetime was determined for each individual eddy, independently from their residence time within the box. The median of these radii is 56 km and the median lifetime is 54 days.

Figure 12 furthermore reveals that on average mooring EB3 is located close to the southern boundary of a stationary cyclonic vortex, which induces east- to northeastward (cross-slope) velocities. In contrast, the surface velocities near EB1 are oriented northwestward (along-slope) and are less impacted by the eddies (Figure 12a). The META analysis supports this view (not shown), as we find a higher fraction of eddy centers passing the EB3 mooring site within 20 km distance (24 eddies) during 1993–2019 compared to EB1, where 17 eddies pass within 20 km distance. We note here that we can only assess the impact of eddies that leave an imprint in the shape of the sea surface and are thus detectable from altimetric data sets like the ones used here. The first baroclinic Rossby radius of deformation is about 20 km in our region of interest (Chelton et al., 1998). Thus, we cannot rule out missing small-scale vortices that are not properly captured in the considered datasets but still affect the mooring records.

During the period of weak and reversed flow with strong vector rotations at EB1 in the beginning of 2018 (highlighted in Figure 4), the local surface velocity field at the mooring sites was influenced by strong eddies

with negative ADT anomalies (Figure 12c). At EB3, strong northward along-slope currents are seen in the absolute geostrophic flow field, but at EB1, currents are rotated to an up-slope direction. South of Goban Spur off the continental slope several dipoles are evident in the ADT field. The eddy field in the whole region exhibits enhanced current velocities during the first half of 2018 (Figure 12c), which is imprinted in our mooring records. We thus note that the current system at our mooring sites is strongly affected by the proximity of deflected NAC pathways and the presence of eddies near the mooring sites, with each of the moorings being affected differently.

5. Summary and Discussion

The analyses presented in this study are based on velocity time series from two moorings installed along the crest of Goban Spur from 2016 to 2019 (Figure 1). The moorings form the eastern extension of the NOAC observatory array at 47°/48°N (Frajka-Williams et al., 2019; Nowitzki et al., 2021; Rhein et al., 2011, 2019). The focus of this study was to quantify the strength and investigate the variability of the top-to-bottom volume transport of the ESC component located over the deeper part (1,500–4,500-m isobaths) of the Goban Spur slope area (Figure 3). We addressed this as the deep EBC. This current component has to our knowledge not yet been analyzed in a systematic way. The shallow slope current contributing to the ESC system (Figure 1) was not covered by the moorings.

5.1. Variability of the Deep EBC at Goban Spur

We found a rather persistent poleward flow of the deep EBC at the shallower mooring EB1, while the flow field at the deeper, offshore position of mooring EB3 was of a more intermittent character and weak on average (e.g., Figure 4). The current field at both mooring sites showed a very different behavior despite their local vicinity, that is, along-slope variations dominated at EB1, while cross-slope variations were more important at EB3 (e.g., Figures 5 and 6). Different characteristics in velocity at stations close to each other were already noted by Pingree and Le Cann (1990), who also described the flow close to the continental slope to be a pole-ward current of barotropic character. Our results do not provide clear evidence of a permanent deep EBC extending from the shelf break to the position of the offshore mooring site EB3, but confirm a persistent along-slope flow at EB1. Embedded into this flow field is what seems to be a counter-current of which we find indications in our repeated LADCP surveys (Figure 3), as well as in the bottom-near current meter installed at mooring EB1 (Figure 4a).

A notable exception from the general flow pattern was the period from January 2018 to May 2018, when currents at EB1 showed high variance, but the flow at EB3 was in a prolonged pole-ward state (Figures 4 and 12c). Current variability at the mooring sites is presumably influenced by the regional eddy field, which is embedded into a complex system of partly meandering surface currents. Eddies derived from sea surface height differences and geostrophic surface velocities showed a stationary character on time scales of weeks to months. They correspond to vortices described in earlier studies with scales ranging from 20 to 100 km that are either stationary or propagate away from the shelf westwards into the interior (e.g., Arhan et al., 1994; Huthnance et al., 2001; Miller et al., 1996; Pingree, 1979; Pingree et al., 1999; Shoosmith et al., 2005; van Aken, 2002). The ADT fields suggest that Goban Spur is an obstacle not only for water approaching from the south along the slope, but also for water that is advected from the north and west in branches of the NAC. The sharp topographic corner at Goban Spur was noted to be favorable for the generation of eddies before (Shoosmith et al., 2005). The dominant cross-slope variation of the current in the upper water column at EB3 is likely evoked by near-stationary eddies or meandering and recirculation of offshore current branches in its vicinity (Figure 12).

5.2. Transport Time Series of the Deep EBC

By scaling the vertically integrated velocities from the moorings with a typical horizontal current width, we have derived a mean northward transport of 3.7 Sv with a standard deviation of 4.6 Sv and a standard error of 0.7 Sv for the mooring period 2017–2019. To our knowledge, this is the first volume flux estimate of the deep EBC in this region. It represents the mean contribution of the deep EBC to the ESC system at Goban Spur. Top-to bottom transports vary in a range between −7.5 and 15.7 Sv. The major uncertainties in

this approach arise from the scaling width and from the assumption of constant flow above and below our uppermost and deepest measurements. Comparisons with independent velocity measurements from LADCP sections conducted during cruises indicate that these uncertainties are up to 0.6 Sv. When extending the mooring-derived transport time series back in time using satellite-derived surface geostrophic velocity fields, we find consistently high variability in the northward transport of the deep EBC, featuring time scales from months to years.

There are only a few other transport calculations for sites in the vicinity of Goban Spur: Pingree and Le Cann (1989) provide a transport estimate for the La Chapelle Bank area upstream of Goban Spur, where they estimate about 1 Sv of transport between the shelf break and the 1,500-m isobath. This increases to 4 Sv for the entire width of the slope. Nowitzki et al. (2021) estimate that a northward transport of 2.2 Sv at the eastern boundary east of 15°W is needed to close the mass balance across the basin-wide width of the 47°/48°N NOAC-section (Rhein et al., 2011, 2019). Our estimate compares well with both numbers, considering that we do not resolve the southward flow west of EB3 that is identified by LADCP measurements or the flow associated with the shallow Slope Current. A combination of all the different transport components covered by the NOAC observational array along 47°/48°N will allow us to infer an integrated estimate regarding the strength of the Atlantic Meridional Overturning Circulation (AMOC) at this latitude (e.g., Frajka-Williams et al., 2019; McCarthy et al., 2020).

5.3. Continuity of the ESC

There remains uncertainty about the continuity of the ESC and its offshore part, the deep EBC, along the European slope. Drogued drifter data and model particle trajectories show clearly the inflow of Atlantic Water from the shallow Slope Current into the North Sea (Marsh et al., 2017). But, Where is the upstream supply route of the inflow? Using altimeter data of a previous ADT product covering the period 1993–2012, Xu et al. (2015) analyzed seasonal variability of the ESC. They created seasonal maps of geostrophic currents from the full length of the altimeter record and removed the overall mean from each map. The authors find a notable seasonal change with a poleward ESC pattern in the winter (November–January) season and weakening of the ESC corresponding to a reversal toward equator-ward flow during the summer (May–July) period. Similar distributions for spring and autumn resembled the 20-year mean state with rather weak flow over the slope region with varying directions. We have analyzed the same seasons over the full length of our updated altimeter dataset and contrast the absolute geostrophic velocities for winter and summer (appendix, Figures C1a and C1c) with respective anomalies referenced to the full period 1993–2019 (appendix, Figures C1b and C1d). The weakening of the ESC expressed by an equatorward flow stands out in the summer season in both, the absolute geostrophic velocities and the geostrophic velocity anomalies. The winterly poleward flow stretching along the slope from the Bay of Biscay to Porcupine Bank, however, emerges only when addressing the respective anomaly distribution (Figure C1b). The winter distribution of the absolute geostrophic velocity fields shows a higher similarity to the overall long-term distribution shown in Figure 12a and previously discussed.

Bower et al. (2002) present two stream function distributions obtained from neutrally buoyant RAFOS floats. The stream function representing the circulation in the upper ocean (~900 m) suggests along-slope flow from the Bay of Biscay until Goban Spur where it recirculates into the ocean interior. The respective stream function for the deeper ocean (about 1,500–1,700-m depth) is inconclusive in our region of interest due to the lack of sufficient data. Regarding our own observations with focus on the deep EBC, we cannot resolve this issue with certainty, although a continuous deep EBC seems unlikely.

In order to consider this question from a different point of view, we include an analysis of Argo float trajectories focused on our mooring period 2016–2019. We split the eastern boundary region into three segments by defining boxes along the slope (see Section 2.5 for a detailed definition of the box outlines). Then, floats were sorted by their occurrence in these boxes. In Figure 13, we show the trajectories of 51 profiling Argo floats that have surfaced in at least one of the three boxes along the continental slope. The northern and central boxes I and II are preferentially reached by floats originating in a latitudinal band stretching from about 45°N to 55°N. They mostly enter the boxes coming from the western basin. These floats follow prominent branches of the NAC as it crosses the Mid-Atlantic Ridge (e.g., Bower & von Appen, 2008; Bower et al., 2002). A preferred northward advection pathway is seen for floats that arrive in the southern box III,

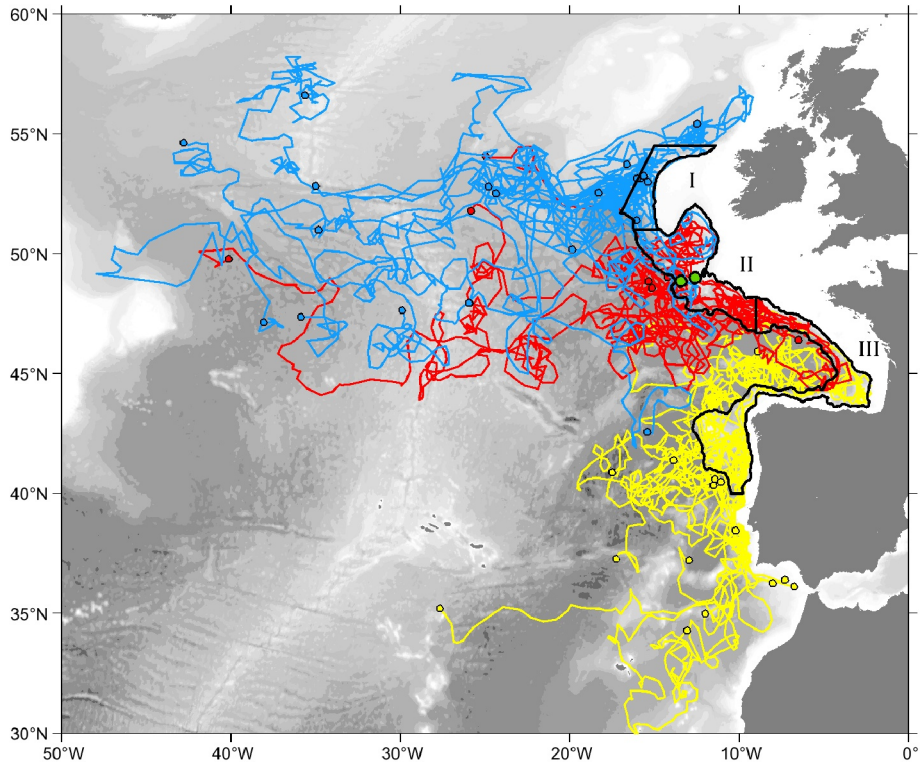

Figure 13. Trajectories of profiling Argo floats that surfaced in the northern box I (blue), middle box II (red) and southern box III (yellow) in the period 2016–2019. Trajectories are drawn from the deployment position (black circle) to the position of the last profile within a box. Black contours denote the boundaries of the boxes (see Section 2.5 for definition). Green dots indicate the positions of the moorings EB1 and EB3.

as they typically originate further south. However, these floats only rarely follow the continental slope on an extended pathway. They rather enter, leave, and reenter the box, which might be caused by flow-topography interaction along the western slope of the Iberian Peninsula and the presence of eddies (e.g., Haynes & Barton, 1990).

In the Bay of Biscay, near-shelf moorings showed a seasonally changing circulation. Le Boyer et al. (2013) found the flow field over the shelf and upper slope to be poleward, with marked seasonality, and steered by the topography. While the summer flow field was directed equatorward on the outer shelf near surface, the flow field over the deeper part of the water column was still poleward. It remains unclear whether these circulation patterns observed at the shelf break can be transferred to the deeper outer-shelf region, since the Argo floats are typically programmed to drift at a parking depth of 1,000 m.

Generally, the Argo trajectories do not show a preferred continuous northward advection path from the eastern subtropical regions of the North Atlantic. They rather confirm our results regarding the intermittent character of the flow at Goban Spur.

5.4. Relation Between Transport of the EBC to the SPG Gyre Strength

In general, the contribution of each gyre to the water masses spreading along the eastern boundary is linked to the extension of the SPG (Häkkinen & Rhines, 2004; Hátún et al., 2005; Holliday, 2003; Johnson et al., 2013; Lozier & Stewart, 2008; Stendardo et al., 2015). However, our results (Figure 11) show no direct link between the SPG index from Hátún and Chafik (2018) and Chafik (2019) and the local dynamics at Goban Spur, confirming previous assessments (Hátún & Chafik, 2018). Another approach to quantify the strength and extension of the SPG, similar to the existing gyre index but based on the regional dynamical conditions in the eastern basin, would be more suitable for comparison and allow more insights into the low-frequency variability of this region, but is beyond the scope of this work. Sensitivity to subtropical and

tropical processes was not tested here and is a topic of subsequent investigations. The continuation of the monitoring program and the transport time series will allow a more in-depth analysis of the relation between the circulation and advection along the eastern boundary and the exchanges between the STG and SPG.

6. Conclusions

The temporal resolution of the mooring record has allowed to analyze the variability in the along-slope flow field, ranging from daily to intraannual and interannual time scales. The meaningful combination of the 2-year mooring record with presently 27 years of surface geostrophic velocities provided a long-term time series for the volume transport of the deep EBC. These results, when furthermore combined with the temperature and salinity records of the two moorings, will contribute to unraveling the origin and variability of the water masses that are advected along the European slope and subsequently modify the adjacent regions, that is, the Northwest European Shelf, the North Sea, the Nordic Seas, and finally the Arctic Ocean.

Appendix A: Mooring Design

Figure A1 presents the instrumental composition of the two moorings EB1 and EB3. Installed sensors are highlighted in color regarding sensor depths and deployment periods.

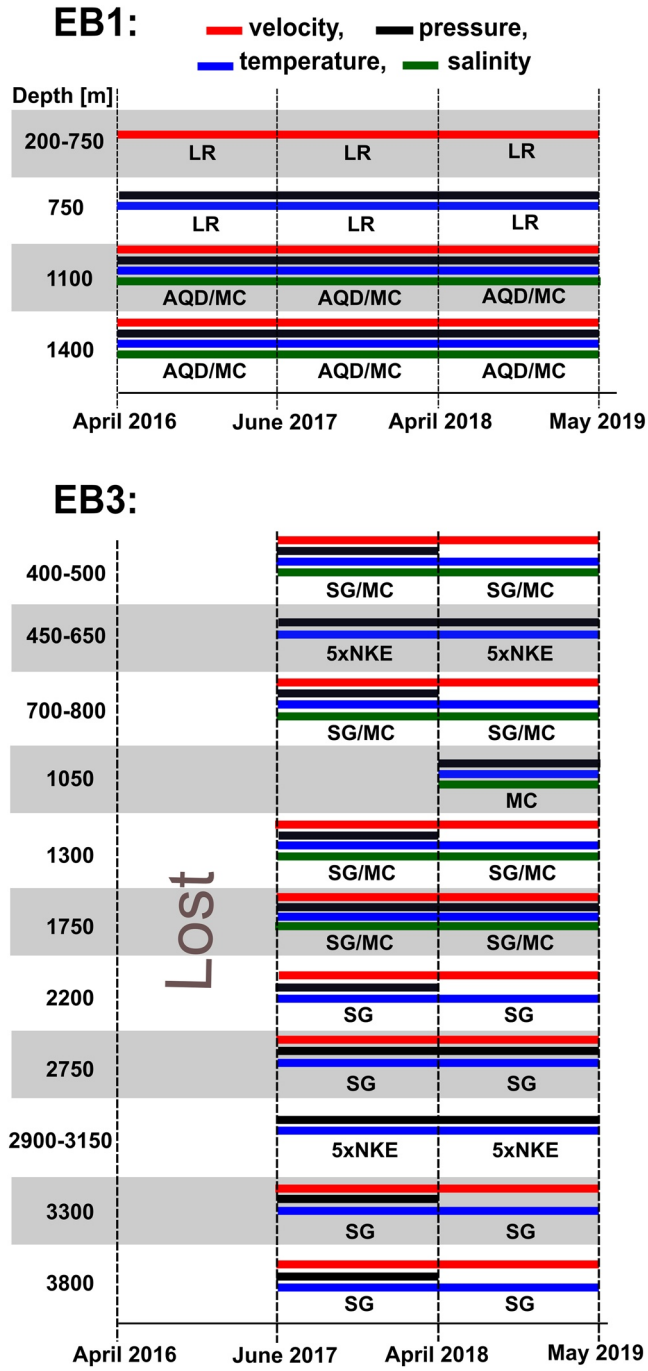

Figure A1. Scheme of the eastern boundary (EB) mooring array design including instrument types nominal instrument depths and measured parameters. LR, Teledyne-RD Instruments Workhorse Longranger Acoustic Doppler Current Profiler; AQD, Nortek Aquadopp Deepwater; SG, Aanderaa Seaguard RCM DW; MC, Seabird 37SM MicroCAT; NKE, NKE Instrumentation temperature loggers.

Appendix B: Repeated Sections

Figure B1 shows the hydrographic distribution regarding temperature, salinity and potential vorticity for four different cruises conducted during 2016 to 2019. Similarly, Figure B2 highlights the along-slope and the cross-slope velocity distribution for each of the four cruises. These are the individual sections that were used for the calculation of the composite sections (see Fig. 2 and 3 in section 3).

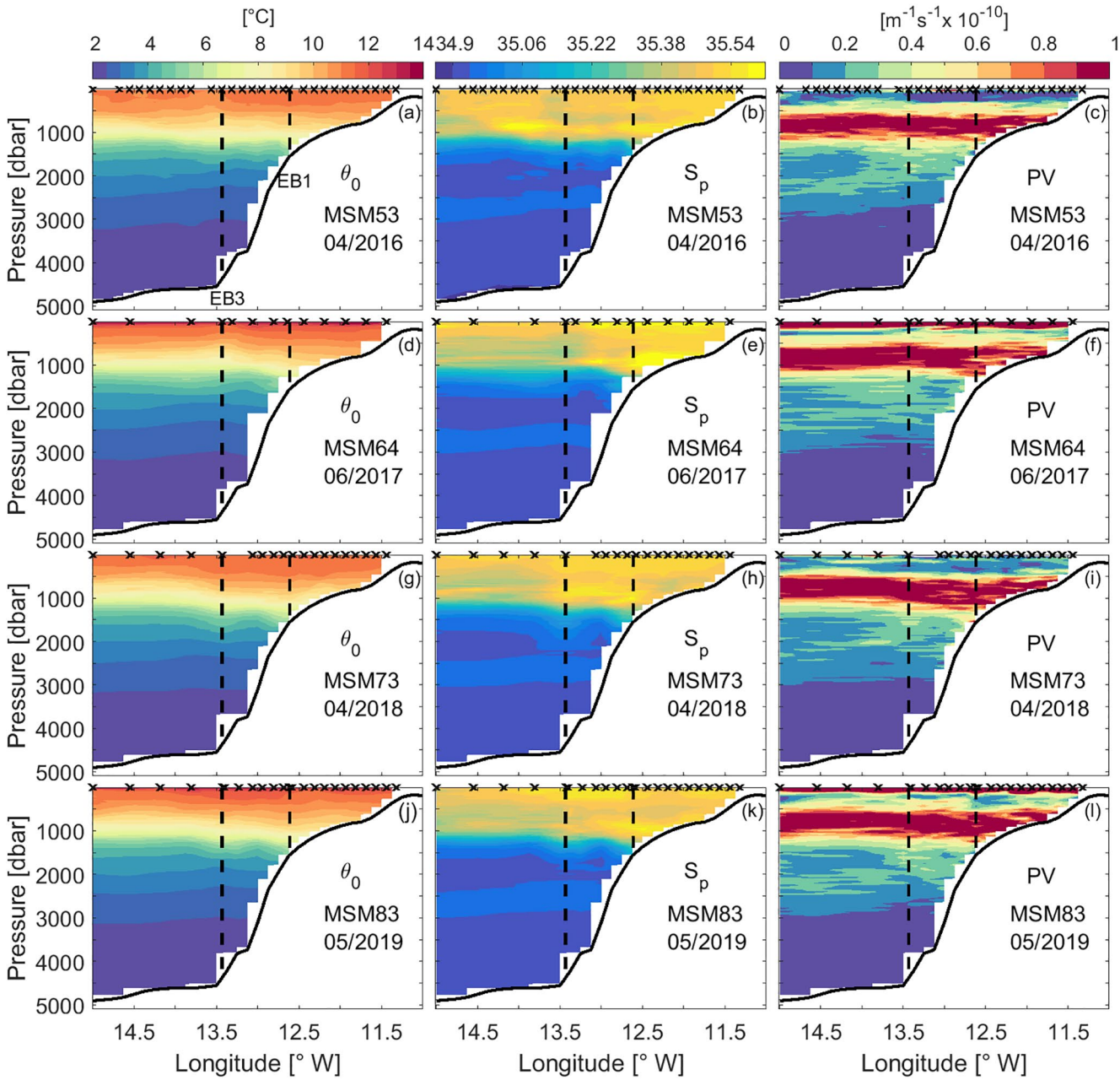

Figure B1. Hydrographic sections of Potential Temperature (left column) θ_0, Practical Salinity S_P (middle column) and Potential Vorticity PV (right column) obtained from four annual CTD surveys. Vertical dashed lines indicate the positions of moorings EB1 and EB3. The crosses at the top of each plot mark the positions of the CTD stations. The repeated cruise track is shown in Figure 1.

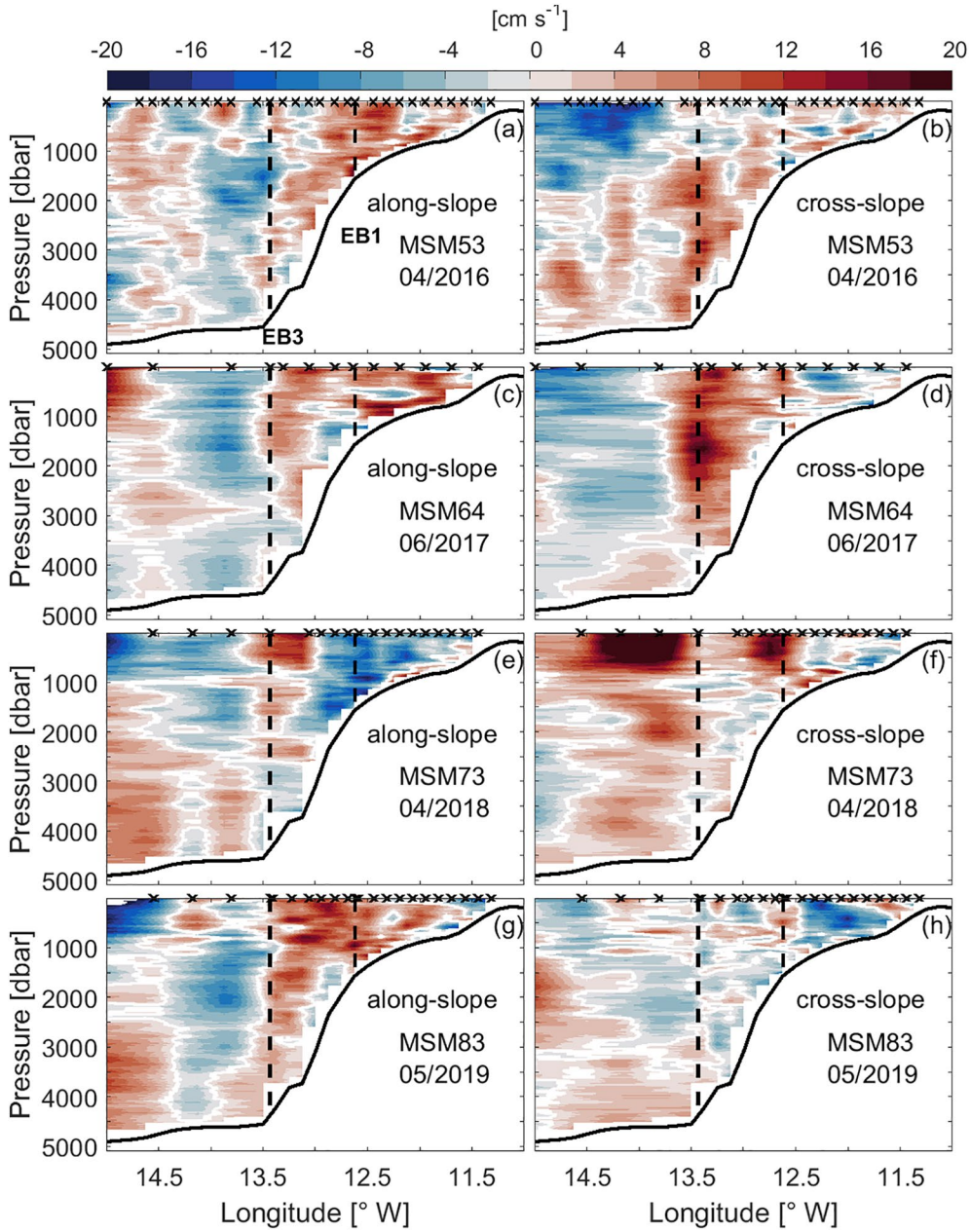

Figure B2. Sections of along-slope (left column) and cross-slope velocity (right column) obtained from four annual CTD surveys. White contours indicate zero velocity. Vertical dashed lines indicate the positions of moorings EB1 and EB3. The crosses at the top of each plot mark the positions of the CTD stations. The repeated cruise track is shown in Figure 1.

Appendix C: Seasonality of ADT and Geostrophic Currents

Figure C1 presents maps showing seasonal changes (mean and anomaly) of absolute dynamic topography (ADT) and geostrophic surface currents during 1993 to 2019.

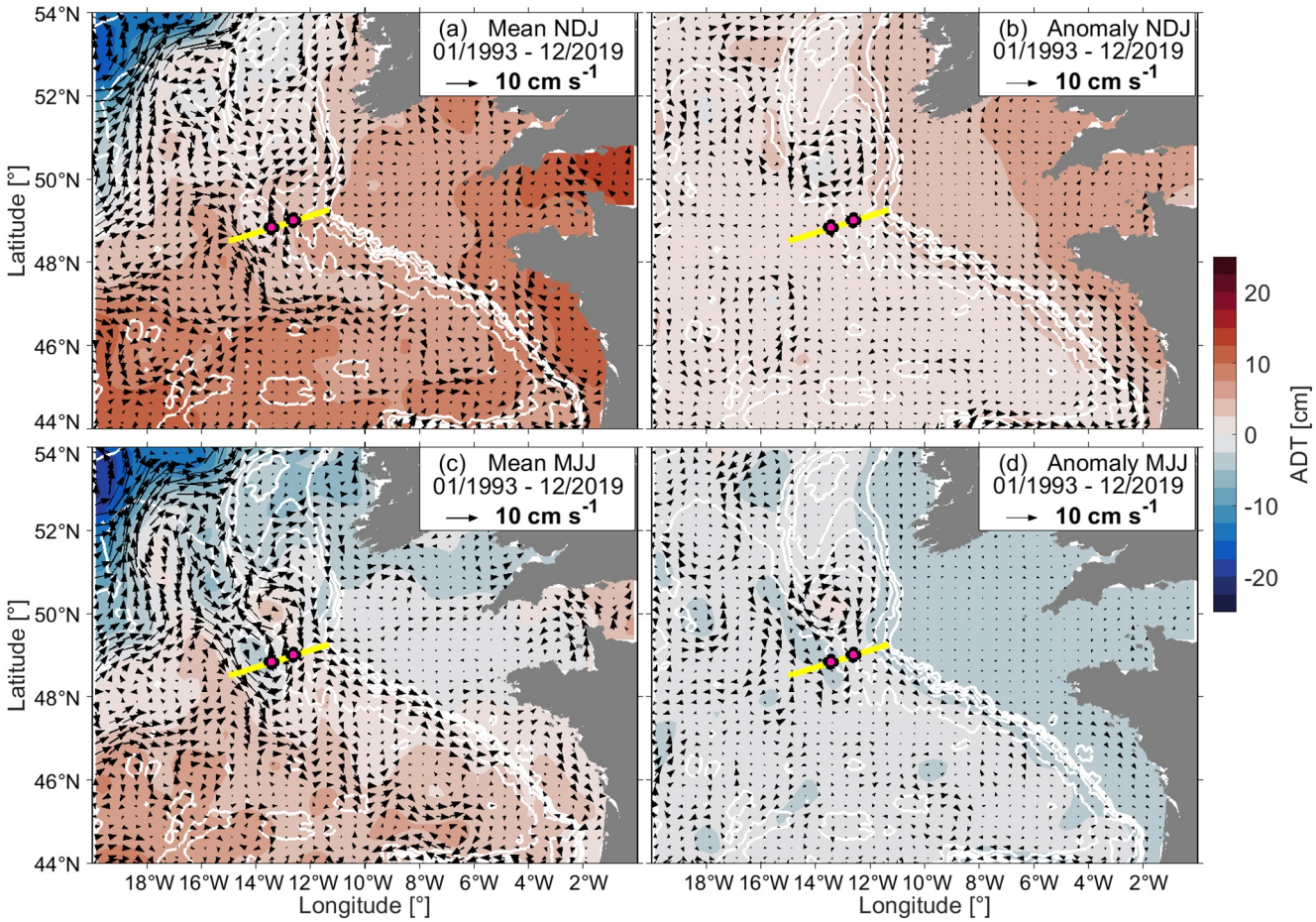

Figure C1. Maps of mean Absolute Dynamic Topography (ADT, colored contours) and geostrophic surface velocities (black arrows) averaged for the winter season (NDJ) and summer season (MJJ). Absolute values for the period are shown in (a) and (c), anomalies referenced to the mean 1993–2019 are shown in (b) and (d). The positions of the moorings are indicated by magenta dots. The yellow line marks the cruise track for the hydrographic section shown in Figure 2. White contour lines indicate the 1,000 m and 4,000 m isobaths.

Appendix D: Contributions of Individual Water Masses to the Deep EBC Transport

The volume transport of the deep EBC can be split into the contributions of the different water masses present at Goban Spur (see summary of relevant water masses in Table 2). Corresponding mean transports and standard deviations are given in Table D1, as well as the layer thickness of each water mass, the mean velocity in each layer and the area used for transport calculation.

Table D1
Mean Along-Slope Velocities, Water Mass Transports With Standard Deviation (std. dev.), Layer Thickness and Area for Transport Calculation for the Different Water Masses Present at Goban Spur

Water mass	Thickness (m)	Average along-slope velocity (cm s^{-1})	Area ($10^6 m^2$)	Average along-slope transport (Sv)	Std. Dev. of transport (Sv)
SPMW	400	3.9	24.8	1.0	0.8
IW	250	3.6	15.5	0.6	0.4
MOW	250	3.1	15.5	0.5	0.4
ULSW	550	2.6	34.1	0.9	1.2
DLSW	450	1.0	17.4	0.2	0.7
LDW	2,300	0.0	44.6	0.0	1.4

Note. SPMW, subpolar mode water; IW, intermediate water; MOW, Mediterranean outflow water; ULSW, upper Labrador sea water; DLSW, deep Labrador sea water; LDW, lower deep water.

Mean velocities are of a similar magnitude in the upper and intermediate layers and decrease in the deep water and toward the bottom. The relative variability of the individual water mass transports in comparison to its mean flow increases with depth: in the upper and intermediate layers, average transports exceed the respective standard deviation. In the deep water, the average transport is very low, but standard deviations still remain at high levels. The bulk of the northward flow occurs in the upper water column and comprises the SPMW, IW, MOW, and ULSW layers. The deep and bottom layers (DLSW and LDW) occupy more than half of the water column (and more than 1/3 of the area for transport calculations), but on average contribute only about 5% to the deep EBC flow. In contrast, the intermediate waters (IW + MOW) contribute 30% of the total transport, although they only occupy a layer of 500 m in thickness.

Data Availability Statement

Ship-based CTD and lowered ADCP data are archived in the PANGAEA data repository accessible at www.pangaea.de. CTD data: Steinfeldt et al. (2020a); Steinfeldt et al. (2020b, 2020c, 2021), LADCP data: Mertens et al. (2020); Mertens et al. (2021a, 2021b). The mooring current meter data and transport time series are published open access in the PANGAEA data repository (Moritz et al., 2021). The altimeter data used in this study (Global Ocean Gridded L4 Sea Surface Heights and Derived Variables Reprocessed, 1993 and ongoing, product identifier: SeaLevel_GLO_PHY_L4_REP_008_047) were obtained from the Copernicus Marine Environmental Monitoring Service (CMEMS; access of the latest update on 26 Jan 2021). The altimetric Mesoscale Eddy Trajectory Atlas (META) products were produced by SSALTO/DUACS and distributed by AVISO+ (https://www.aviso.altimetry.fr) with support from CNES, in collaboration with Oregon State University with support from NASA. The particular data set version "META2.0 DT" was accessed on 24 Feb 2021. The ERA5 wind data were retrieved from Copernicus Climate Change Service Climate Data Store (CDS), accessed on 21 Oct 2020 (https://cds.climate.copernicus.eu). The Argo data were retrieved from the Argo GDAC: doi:10.17882/81942182#66561. The North Atlantic subpolar gyre index, version 3.0, has been obtained from Chafik (2019), web site accessed on 04 Feb 2021.

Acknowledgments
The observations from the years 2016–2018 and respective analysis are part of the RACE (Regional Atlantic Circulation and Global Change) and RACE/Synthesis programs, both funded by the German Ministry of Education and Research BMBF (grants 03F0605C, 03F0561C to M. Rhein, grant 03F0730A to B. Klein, grant 03F0824A to M. Rhein and D. Kieke). The 2019 cruise was funded by the German Research Foundation (DFG) under grant GPF-18-1_43 to M. Rhein and D. Kieke. R. Steinfeldt (IUP) processed and calibrated the CTD data during the cruises, while the lowered ADCP data of the different cruises were processed by A. Rössler (IUP, MSM53, MSM64), F. Wischnewski (IUP, MSM73). The authors acknowledge the assistance and technical support from the group's teams, in particular Anja Schneehorst (BSH), Hans-Hermann Uhde (BSH), and Wolfgang Böke (IUP), and the ship crews of RV Maria S. Merian. This study has been conducted using E.U. Copernicus Marine Service Information. This study contains modified Copernicus Climate Change Service Information (2020). Neither the European Commission nor ECMWF is responsible for any use that may be made of the Copernicus information or data it contains. They thank the two reviewers for their thoughtful comments and suggestions.

References

Argo. (2019). *Argo float data and metadata from global data assembly centre (Argo GDAC): Snapshot of Argo GDAC of August 8th, 2019 [Data set]*. https://doi.org/10.17882/42182#66561

Arhan, M., Colin De Verdiére, A., & Mémery, L. (1994). The eastern boundary of the subtropical North Atlantic. *Journal of Physical Oceanography*, *24*(6), 1295–1316. https://doi.org/10.1175/1520-0485(1994)024<1295:TEBOTS>2.0.CO;2

AVISO. (2021). *Mesoscale eddy trajectory Atlas product handbook, SALP-MU-P-EA-23126-CLS, 3 rev 3 (Dataset)*. Retrieved from https://www.aviso.altimetry.fr/en/data/products/value-added-products/global-mesoscale-eddy-trajectory-product.html

Bower, A. S., Cann, B. L., Rossby, T., Zenk, W., Gould, J., Speer, K., et al. (2002). Directly measured mid-depth circulation in the northeastern North Atlantic Ocean. *Nature*, *419*(6907), 603–607. https://doi.org/10.1038/nature01078

Bower, A. S., & von Appen, W.-J. (2008). Interannual variability in the pathways of the North Atlantic Current over the Mid-Atlantic Ridge and the impact of topography. *Journal of Physical Oceanography*, *38*(1), 104–120. https://doi.org/10.1175/2007JPO3686.1

Chafik, L. (2019). *North Atlantic subpolar gyre index. Dataset version 3.0. Bolin center database [Data set]*. https://doi.org/10.17043/chafik-2019-3

Chelton, D. B., deSzoeke, R. A., Schlax, M. G., El Naggar, K., & Siwertz, N. (1998). Geographical variability of the first baroclinic Rossby radius of deformation. *Journal of Physical Oceanography*, *28*(3), 433–460. https://doi.org/10.1175/1520-0485(1998)028<0433:GVOTFB>2.0.CO;2

Chelton, D. B., Schlax, M. G., & Samelson, R. M. (2011). Global observations of nonlinear mesoscale eddies. *Progress in Oceanography*, *91*, 167–216. https://doi.org/10.1016/j.pocean.2011.01.002

Copernicus Climate Change Service (C3S). (2017). *ERA5: Fifth generation of ECMWF atmospheric reanalyzes of the global climate*. Copernicus Climate Change Service Climate Data Store (CDS). Retrieved from https://cds.climate.copernicus.eu/cdsapp#!/home

Egbert, G. D., & Erofeeva, S. Y. (2002). Efficient inverse modeling of barotropic ocean tides. *Journal of Atmospheric and Oceanic Technology*, *19*(2), 183–204. https://doi.org/10.1175/1520-0426(2002)019<0183:eimobo>2.0.co;2

Erwan, T., Finlay, C., Beggan, C., Alken, P., Aubert, J., Barrois, O., & Zvereva, T. (2015). International geomagnetic reference field: The 12th generation. *Earth, Planets and Space*, *67*, 79. https://doi.org/10.1186/s40623-015-0228-9

Frajka-Williams, E., Ansorge, I. J., Baehr, J., Bryden, H. L., Chidichimo, M. P., Cunningham, S. A., et al. (2019). Atlantic meridional overturning circulation: Observed transport and variability. *Frontiers in Marine Science*, *6*, 260. https://doi.org/10.3389/fmars.2019.00260

Häkkinen, S., & Rhines, P. B. (2004). Decline of subpolar North Atlantic circulation during the 1990s. *Science*, *304*(5670), 555–559. https://doi.org/10.1126/science.1094917

Häkkinen, S., & Rhines, P. B. (2009). Shifting surface currents in the northern North Atlantic Ocean. *Journal of Geophysical Research: Oceans*, *114*(C4). https://doi.org/10.1029/2008JC004883

Hátún, H., & Chafik, L. (2018). On the recent ambiguity of the North Atlantic subpolar gyre index. *Journal of Geophysical Research: Oceans*, *123*(8), 5072–5076. https://doi.org/10.1029/2018JC014101

Hátún, H., Sandø, A. B., Drange, H., Hansen, B., & Valdimarsson, H. (2005). Influence of the Atlantic subpolar gyre on the thermohaline circulation. *Science*, *309*(5742), 1841–1844. https://doi.org/10.1126/science.1114777

Haynes, R., & Barton, E. D. (1990). A poleward flow along the Atlantic coast of the Iberian peninsula. *Journal of Geophysical Research: Oceans*, *95*(C7), 11425–11441. https://doi.org/10.1029/JC095iC07p11425

Holliday, N. P. (2003). Air-sea interaction and circulation changes in the northeast Atlantic. *Journal of Geophysical Research*, *108*(C8). https://doi.org/10.1029/2002JC001344

Holliday, N. P., Bersch, M., Berx, B., Chafik, L., Cunningham, S., Florindo-López, C., et al. (2020). Ocean circulation causes the largest freshening event for 120 years in eastern subpolar North Atlantic. *Nature Communications*, *11*(585). https://doi.org/10.1038/s41467-020-14474-y

Huthnance, J. M., Coelho, H., Griffiths, C. R., Knight, P. J., Rees, A. P., Sinha, B., et al. (2001). Physical structures, advection and mixing in the region of Goban Spur. *Deep Sea Research Part II: Topical Studies in Oceanography*, *48*(14–15), 2979–3021. https://doi.org/10.1016/S0967-0645(01)00030-3

Iorga, M. C., & Lozier, M. S. (1999). Signatures of the Mediterranean outflow from a North Atlantic climatology: 1. Salinity and density fields. *Journal of Geophysical Research: Oceans*, *104*(C11), 25985–26009. https://doi.org/10.1029/1999JC900115

Johnson, C., Inall, M., & Häkkinen, S. (2013). Declining nutrient concentrations in the northeast Atlantic as a result of a weakening Subpolar Gyre. *Deep Sea Research Part I: Oceanographic Research Papers*, *82*, 95–107. https://doi.org/10.1016/j.dsr.2013.08.007

Kieke, D., Klein, B., Stramma, L., Rhein, M., & Koltermann, K. P. (2009). Variability and propagation of Labrador Sea Water in the southern subpolar North Atlantic. *Deep Sea Research Part I: Oceanographic Research Papers*, *56*(10), 1656–1674. https://doi.org/10.1016/j.dsr.2009.05.010

Le Boyer, A., Charria, G., Le Cann, B., Lazure, P., & Marié, L. (2013). Circulation on the shelf and the upper slope of the Bay of Biscay. *Continental Shelf Research*, *55*, 97–107. https://doi.org/10.1016/j.csr.2013.01.006

Lherminier, P., Mercier, H., Huck, T., Gourcuff, C., Perez, F. F., Morin, P., et al. (2010). The Atlantic Meridional Overturning Circulation and the subpolar gyre observed at the A25-OVIDE section in June 2002 and 2004. *Deep Sea Research Part I: Oceanographic Research Papers*, *57*(11), 1374–1391. https://doi.org/10.1016/j.dsr.2010.07.009

Lilly, J. (2019). *jLab: A data analysis package for Matlab; v. 1.6.6*. Retrieved from http://www.jmlilly.net/software

Lozier, M. S., & Stewart, N. M. (2008). On the temporally varying northward penetration of Mediterranean Overflow Water and eastward penetration of Labrador Sea Water. *Journal of Physical Oceanography*, *38*(09), 2097–2103. https://doi.org/10.1175/2008JPO3908.1

Marsh, R., Haigh, I. D., Cunningham, S. A., Inall, M. E., Porter, M., & Moat, B. I. (2017). Large-scale forcing of the European Slope Current and associated inflows to the North Sea. *Ocean Science*, *13*(2), 315–335. https://doi.org/10.5194/os-13-315-2017

McCarthy, G. D., Brown, P. J., Flagg, C. N., Goni, G., Houpert, L., Hughes, C. W., et al. (2020). Sustainable observations of the AMOC: Methodology and technology. *Reviews of Geophysics*, *58*(1), e2019RG000654. https://doi.org/10.1029/2019RG000654

McCartney, M. S., & Mauritzen, C. (2001). On the origin of the warm inflow to the Nordic Seas. *Progress in Oceanography*, *51*(1), 125–214. https://doi.org/10.1016/S0079-6611(01)00084-2

McDougall, T. J., & Barker, P. M. (2011). *Getting started with TEOS-10 and the Gibbs Seawater (GSW) oceanographic toolbox* (pp. 1–28). SCOR/IAPSO WG.

Mertens, C., Kieke, D., & Rhein, M. (2021a). *Lowered Acoustic Doppler Current Profiler (LADCP, 300 kHz) current measurements collected during MARIA S. MERIAN cruise MSM73 [Data set]*. Retrieved from https://doi.pangaea.de/10.1594/PANGAEA.926833

Mertens, C., Kieke, D., & Rhein, M. (2021b). *Lowered Acoustic Doppler Current Profiler (LADCP, 300 kHz) current measurements collected during MARIA S. MERIAN cruise MSM83 [Data set]*. Retrieved from https://doi.pangaea.de/10.1594/PANGAEA.927113

Mertens, C., Rhein, M., Roessler, A., Kieke, D., & Nowitzki, H. (2020). *Lowered ADCP data at N in the subpolar North atlantic [Data set]*. Retrieved from https://doi.pangaea.de/10.1594/PANGAEA.922859

Mertens, C., Rhein, M., Walter, M., Böning, C. W., Behrens, E., Kieke, D., et al. (2014). Circulation and transports in the Newfoundland Basin, western subpolar North Atlantic. *Journal of Geophysical Research: Oceans*, *119*(11), 7772–7793. https://doi.org/10.1002/2014JC010019

Miller, P., Groom, S., McManus, A., Selley, J., Woolfenden, J., Blewett, J., & Osborne, L. (1996). *Remote sensing activities in OMEX. (OMEX final report B)*.

Moritz, M., Jochumsen, K., Kieke, D., Klein, B., Klein, H., Köllner, M., & Rhein, M. (2021). *Current meter measurement data and volume transport time series from deep-sea moorings deployed in the North Atlantic Eastern Boundary (EB) region at Goban Spur [Data set]*. PANGAEA. Retrieved from https://doi.pangaea.de/10.1594/PANGAEA.932566

New, A., Barnard, S., Herrmann, P., & Molines, J.-M. (2001). On the origin and pathway of the saline inflow to the Nordic Seas: Insights from models. *Progress in Oceanography*, *48*(2), 255–287. https://doi.org/10.1016/S0079-6611(01)00007-6

NOAA. (1988). Digital relief of the surface of the Earth. In *Data announcement 88-MGG-02*. Boulder, CO: NOAA, National Geophysical Data Center.

Nowitzki, H., Rhein, M., Roessler, A., Kieke, D., & Mertens, C. (2021). Trends and transport variability of the circulation in the subpolar eastern North Atlantic. *Journal of Geophysical Research: Oceans*, *126*. https://doi.org/10.1029/2020JC016693

Percival, D. B., & Walden, A. T. (1993). *Spectral analysis for physical applications*. Cambridge University Press. https://doi.org/10.1017/CBO9780511622762

Pingree, R. D. (1979). Baroclinic eddies bordering the Celtic Sea in late summer. *Journal of the Marine Biological Association of the United Kingdom*, *59*(3), 689–703. https://doi.org/10.1017/S0025315400045677

Pingree, R. D. (1993). Flow of surface waters to the west of the British Isles and in the Bay of Biscay. *Deep Sea Research Part II: Topical Studies in Oceanography*, *40*(1), 369–388. https://doi.org/10.1016/0967-0645(93)90022-F

Pingree, R. D. (2005). North Atlantic and North Sea climate change: Curl up, shut down, NAO and Ocean Colour. *Journal of the Marine Biological Association of the United Kingdom*, *85*(7), 1301–1315. https://doi.org/10.1017/S0025315405012488

Pingree, R. D., & Le Cann, B. (1989). Celtic and Armorican slope and shelf residual currents. *Progress in Oceanography*, *23*(4), 303–338. https://doi.org/10.1016/0079-6611(89)90003-7

Pingree, R. D., & Le Cann, B. (1990). Structure, strength and seasonality of the slope currents in the Bay of Biscay region. *Journal of the Marine Biological Association of the United Kingdom*, *70*(4), 857–885. https://doi.org/10.1017/S0025315400059117

Pingree, R. D., Sinha, B., & Griffiths, C. R. (1999). Seasonality of the European slope current (Goban Spur) and ocean margin exchange. *Continental Shelf Research*, *19*(7), 929–975. https://doi.org/10.1016/S0278-4343(98)00116-2

Reid, J. L. (1979). On the contribution of the Mediterranean Sea outflow to the Norwegian-Greenland Sea. *Deep Sea Research Part A: Oceanographic Research Papers*, *26*(11), 1199–1223. https://doi.org/10.1016/0198-0149(79)90064-5

Rhein, M., Kieke, D., Hüttl-Kabus, S., Roessler, A., Mertens, C., Meissner, R., et al. (2011). Deep water formation, the subpolar gyre, and the meridional overturning circulation in the subpolar North Atlantic. *Deep Sea Research Part II: Topical Studies in Oceanography*, *58*(17), 1819–1832. https://doi.org/10.1016/j.dsr2.2010.10.061

Rhein, M., Kieke, D., & Steinfeldt, R. (2015). Advection of North Atlantic deep water from the Labrador Sea to the southern hemisphere. *Journal of Geophysical Research: Oceans*, *120*(4), 2471–2487. https://doi.org/10.1002/2014JC010605

Rhein, M., Mertens, C., & Roessler, A. (2019). Observed transport decline at N, western Atlantic. *Journal of Geophysical Research: Oceans*, *124*(7), 4875–4890. https://doi.org/10.1029/2019JC014993

Roessler, A., Rhein, M., Kieke, D., & Mertens, C. (2015). Long-term observations of North Atlantic Current transport at the gateway between western and eastern Atlantic. *Journal of Geophysical Research: Oceans*, *120*, 4003–4027. https://doi.org/10.1002/2014JC010662

Rossby, T. (1996). The North Atlantic Current and surrounding waters: At the crossroads. *Reviews of Geophysics*, *34*(4), 463–481. https://doi.org/10.1029/96RG02214

Schlax, M. G., & Chelton, D. B. (2016). The "growing method" of eddy identification and tracking in two and three dimensions (Tech. Rep.). College of Earth. Corvallis, OR: Ocean and Atmospheric Sciences, Oregon State University. (obtained from AVISO, aviso@aviso.fr).

Shoosmith, D., Richardson, P., Bower, A., & Rossby, H. (2005). Discrete eddies in the northern North Atlantic as observed by looping RAFOS floats. *Deep Sea Research Part II: Topical Studies in Oceanography*, *52*(3), 627–650. https://doi.org/10.1016/j.dsr2.2004.12.011

Steinfeldt, R., Kieke, D., & Rhein, M. (2020a). *Physical oceanography during Maria S. Merian cruise MSM53 [Data set]*. https://doi.org/10.1594/PANGAEA.910842

Steinfeldt, R., Kieke, D., & Rhein, M. (2020b). *Physical oceanography during Maria S. Merian cruise MSM64 [Data set]*. https://doi.org/10.1594/PANGAEA.923550

Steinfeldt, R., Kieke, D., & Rhein, M. (2020c). *Physical oceanography during Maria S. Merian cruise MSM73 [Data set]*. https://doi.org/10.1594/PANGAEA.923565

Steinfeldt, R., Kieke, D., & Rhein, M. (2021). *Physical oceanography during Maria S. Merian cruise MSM83 [Data set]*. Retrieved from https://doi.pangaea.de/10.1594/PANGAEA.927168

Stendardo, I., Kieke, D., Rhein, M., Gruber, N., & Steinfeldt, R. (2015). Interannual to decadal oxygen variability in the mid-depth water masses of the eastern North Atlantic. *Deep Sea Research Part I: Oceanographic Research Papers*, *95*, 85–98. https://doi.org/10.1016/j.dsr.2014.10.009

Stendardo, I., Rhein, M., & Steinfeldt, R. (2020). The North Atlantic Current and its volume and freshwater transports in the subpolar North Atlantic, time period 1993–2016. *Journal of Geophysical Research: Oceans*, *125*(9), e2020JC016065. https://doi.org/10.1029/2020JC016065

Sy, A., Rhein, M., Lazier, J. R. N., Koltermann, K. P., Meincke, J., Putzka, A., & Bersch, M. (1997). Surprisingly rapid spreading of newly formed intermediate waters across the North Atlantic Ocean. *Nature*, *386*, 675–679. https://doi.org/10.1038/386675a0

Taburet, G., Sanchez-Roman, A., Ballarotta, M., Pujol, M.-I., Legeais, J.-F., Fournier, F., et al. (2019). DUACS DT2018: 25 years of reprocessed sea level altimetry products. *Ocean Science*, *15*(5), 1207–1224. https://doi.org/10.5194/os-15-1207-2019

Talley, L. D., & McCartney, M. S. (1982). Distribution and circulation of Labrador sea water. *Journal of Physical Oceanography*, *12*(11), 1189–1205. https://doi.org/10.1175/1520-0485(1982)012<1189:DACOLS>2.0.CO;2

Thomson, D. J. (1982). Spectrum estimation and harmonic analysis. *Proceedings of the IEEE*, *70*(9), 1055–1096. https://doi.org/10.1109/PROC.1982.12433

Thurnherr, A. (2018). *How to process LADCP data with the LDEO software, Versions IX.7 – IX.13 (Tech. Rep.)*. Retrieved from http://www.ldeo.columbia.edu/cgi-bin/ladcp-cgi-bin/hgwebdir.cgi/LDEOIX

Ullgren, J. E., & White, M. (2010). Water mass interaction at intermediate depths in the southern Rockall Trough, northeastern North Atlantic. *Deep Sea Research Part I: Oceanographic Research Papers*, *57*(2), 248–257. https://doi.org/10.1016/j.dsr.2009.11.005

van Aken, H. M. (2000). The hydrography of the mid-latitude northeast Atlantic Ocean I: The deep water masses. *Deep Sea Research Part I: Oceanographic Research Papers*, *47*(5), 757–788. https://doi.org/10.1016/S0967-0637(99)00092-8

van Aken, H. M. (2002). Surface currents in the Bay of Biscay as observed with drifters between 1995 and 1999. *Deep Sea Research Part I: Oceanographic Research Papers*, *49*(6), 1071–1086. https://doi.org/10.1016/S0967-0637(02)00017-1

van Aken, H. M., Maas, L. R. M., & van Haren, H. (2005). Observations of inertial wave events near the continental slope off Goban Spur. *Journal of Physical Oceanography*, *35*(8), 1329–1340. https://doi.org/10.1175/JPO2769.1

Visbeck, M. (2002). Deep velocity profiling using lowered acoustic Doppler current profilers: Bottom track and inverse solutions. *Journal of Atmospheric and Oceanic Technology*, *19*(5), 794–807. https://doi.org/10.1175/1520-0426(2002)019<0794:DVPULA>2.0.CO;2

White, M., & Bowyer, P. (1997). The shelf-edge current north-west of Ireland. *Annales Geophysicae*, *15*(8), 1076–1083. https://doi.org/10.1007/s00585-997-1076-0

Williams, S., Petersen, M., Bremer, P.-T., Hecht, M., Pascucci, V., Ahrens, J., et al. (2011). Adaptive extraction and quantification of geophysical vortices. *IEEE Transactions on Visualization and Computer Graphics*, *17*(12), 2088–2095. https://doi.org/10.1109/TVCG.2011.162

Witt, M. J., & Godley, B. J. (2007). A step towards seascape scale conservation: Using vessel monitoring systems (VMS) to map fishing activity. *PloS One*, *2*(10), e1111. https://doi.org/10.1371/journal.pone.0001111

Xu, W., Miller, P. I., Quartly, G. D., & Pingree, R. D. (2015). Seasonality and interannual variability of the European Slope Current from 20 years of altimeter data compared with in situ measurements. *Remote Sensing of Environment*, *162*, 196–207. https://doi.org/10.1016/j.rse.2015.02.008

Zantopp, R., Fischer, J., Visbeck, M., & Karstensen, J. (2017). From interannual to decadal: 17 years of boundary current transports at the exit of the Labrador Sea. *Journal of Geophysical Research: Oceans*, *122*, 1724–1748. https://doi.org/10.1002/2016JC012271